**Astronomy & Astrophysics**

Special issue

# *Gaia* Data Release 3

## Properties and validation of the radial velocities

D. Katz[1],[⋆], P. Sartoretti[1], A. Guerrier[2], P. Panuzzo[1], G. M. Seabroke[3], F. Thévenin[4], M. Cropper[3], K. Benson[3], R. Blomme[5], R. Haigron[1], O. Marchal[6], M. Smith[3], S. Baker[3], L. Chemin[7], Y. Damerdji[8],[9], M. David[10], C. Dolding[3], Y. Frémat[5], E. Gosset[9],[11], K. Janßen[12], G. Jasniewicz[13], A. Lobel[5], G. Plum[1], N. Samaras[5],[14], O. Snaith[1], C. Soubiran[15], O. Vanel[1], T. Zwitter[16], T. Antoja[17], F. Arenou[1], C. Babusiaux[18],[1], N. Brouillet[15], E. Caffau[1], P. Di Matteo[1], C. Fabre[19],[2], C. Fabricius[17], F. Fragkoudi[20], M. Haywood[1], H. E. Huckle[3], C. Hottier[1], Y. Lasne[21],[2], N. Leclerc[1], A. Mastrobuono-Battisti[1],[22], F. Royer[1], D. Teyssier[23], J. Zorec[24], F. Crifo[1], A. Jean-Antoine Piccolo[2], C. Turon[1], and Y. Viala[1]

*(Affiliations can be found after the references)*

**ABSTRACT**

*Context. Gaia* Data Release 3 (*Gaia* DR3) contains the second release of the combined radial velocities. It is based on the spectra collected during the first 34 months of the nominal mission. The longer time baseline and the improvements of the pipeline made it possible to push the processing limit from $G_{RVS} = 12$ in *Gaia* DR2 to $G_{RVS} = 14$ mag.
*Aims.* We describe the new functionalities implemented for *Gaia* DR3, the quality filters applied during processing and post-processing, and the properties and performance of the published velocities.
*Methods.* For *Gaia* DR3, several functionalities were upgraded or added to the spectroscopic pipeline. The calibrations were improved in order to better model the temporal evolution of the straylight and of the instrumental point spread function (PSF). The overlapped spectra, which were mostly discarded in *Gaia* DR2, are now handled by a dedicated module. The hot star template mismatch, which prevented publication of hot stars in *Gaia* DR2, is largely mitigated now, down to $G_{RVS} = 12$ mag. The combined radial velocity of stars brighter than or equal to $G_{RVS} = 12$ mag is calculated in the same way as in *Gaia* DR2, that is, as the median of the epoch radial velocity time series. The combined radial velocity of the fainter stars is measured from the average of the cross-correlation functions.
*Results. Gaia* DR3 contains the combined radial velocities of 33 812 183 stars. With respect to *Gaia* DR2, the temperature interval has been expanded from $T_{eff} \in [3600, 6750]$ K to $T_{eff} \in [3100, 14\,500]$ K for the bright stars ($G_{RVS} \leq 12$ mag) and $[3100, 6750]$ K for the fainter stars. The radial velocities sample a significant part of the Milky Way: they reach a few kiloparsecs beyond the Galactic centre in the disc and up to about 10−15 kpc vertically into the inner halo. The median formal precision of the velocities is 1.3 km s$^{-1}$ at $G_{RVS} = 12$ and 6.4 km s$^{-1}$ at $G_{RVS} = 14$ mag. The velocity zeropoint exhibits a small systematic trend with magnitude that starts around $G_{RVS} = 11$ mag and reaches about 400 m s$^{-1}$ at $G_{RVS} = 14$ mag. A correction formula is provided that can be applied to the published data. The *Gaia* DR3 velocity scale agrees satisfactorily with APOGEE, GALAH, GES, and RAVE; the systematic differences mostly remain below a few hundred m s$^{-1}$. The properties of the radial velocities are also illustrated with specific objects: open clusters, globular clusters, and the Large Magellanic Cloud. For example, the precision of the data allows mapping the line-of-sight rotational velocities of the globular cluster 47 Tuc and of the Large Magellanic Cloud.

**Key words.** techniques: spectroscopic – techniques: radial velocities – catalogs – surveys

## 1. Introduction

The pioneering space astrometry mission HIPPARCOS (Perryman et al. 1997) was equipped with a two-band photometer, but no spectrograph. Radial velocities were collected from the ground to complement HIPPARCOS proper motions and provide the third component of the velocity vectors. A huge observing endeavour was conducted in particular with the COrrelation-RAdial-VELocities (CORAVEL) spectrographs, which resulted in the publication of new radial velocity measurements for about 13 500 F-G dwarfs (the Geneva-Copenhagen Survey; Nordström et al. 2004) and more than 6500 K-M giants (Famaey et al. 2005), representing more than 15% of the HIPPARCOS catalogue in total. The radial velocity coverage of the HIPPARCOS (Perryman et al. 1997; van Leeuwen 2007) and *Tycho* catalogues (Hoeg et al. 1997; Høg et al. 2000) was further improved by the large spectroscopic surveys initiated at

the beginning of the millennium, such as the RAdial Velocity Experiment (RAVE; Steinmetz 2003; Steinmetz et al. 2006, 2020b). Because of the very large number of sources targeted by *Gaia*, about 1.5 billion, or four orders of magnitude more than HIPPARCOS, it would have been extremely complex and expensive, if not impossible, to observe 10−15% of its targets from the ground. The Radial Velocity Spectrometer (RVS) was therefore included in the *Gaia* payload early in the mission design (Perryman et al. 2001; Katz et al. 2004; Cropper et al. 2018).

The RVS exposure time is 13.2 s per transit, combining the three spectra acquired at each crossing of the RVS focal plane. The collected signal allows deriving single-epoch radial velocities of G-K type stars down to $G_{RVS} \sim 12-13$ mag. For fainter sources, it is necessary to accumulate and combine observations. The second *Gaia* data release (*Gaia* DR2) was based on the first 22 months of the mission (Gaia Collaboration 2018). It was also the first data release containing radial velocities, and for this premiere, the measurement and publication of the

---

⋆ Corresponding author: D. Katz, e-mail: `david.katz@obspm.fr`

line-of-sight velocities were limited to $G_{RVS}$ = 12 mag (Sartoretti et al. 2018; Katz et al. 2019). The Early Third *Gaia* Data Release (*Gaia* EDR3) contained no new radial velocities, but for a convenient use of the database, it included a copy of the *Gaia* DR2 radial velocities. The re-publication of the data also provided the opportunity of re-examining the reliability of the measurements (in particular the possible contaminations by bright neighbours) and led to the rejection of slightly fewer than 15 000 stars (Seabroke et al. 2021).

The Third *Gaia* Data Release (*Gaia* DR3) is based on 34 months of data (Gaia Collaboration 2023c), that is, it adds 12 months to *Gaia* DR2 and therefore a proportional number of observations per source. The number of spectroscopic observations in *Gaia* DR3 is further increased by a new functionality that deblends the overlapping spectra (Seabroke et al., in prep.), while most of them were discarded in *Gaia* DR2. As a consequence, *Gaia* DR3 extends to two magnitudes fainter than *Gaia* DR2 and contains 33 812 183 combined radial velocities. The radial velocities of all sources down to the RVS limiting magnitude of $G_{RVS} \sim 16$ mag are to be published in the Fourth *Gaia* Data Release (*Gaia* DR4), which should process 66 months of data.

This paper is devoted to the description and validation of the radial velocities published in *Gaia* DR3. Two companion papers discuss specific aspects of the *Gaia* DR3 radial velocities. Blomme et al. (2023) and Damerdji et al. (in prep.) describe the dedicated methods that were implemented to derive the radial velocities of hot stars and double-line spectroscopic binaries, respectively. Additionally, three articles present the other products of the spectroscopic pipeline: $G_{RVS}$ magnitudes (Sartoretti et al. 2023), rotational broadening (Frémat et al. 2023), and spectra (Seabroke et al., in prep.). Finally, Babusiaux et al. (2023) present a global overview of the validation and properties of the *Gaia* DR3 data, including the spectroscopic products.

The paper is structured as follows. Section 2 recalls the main characteristics of the RVS. Section 3 provides an overview of the spectroscopic pipeline and summarises the new functionalities implemented to produce *Gaia* DR3. Section 4 presents the filters that were applied on the input data during the processing and during the validation phase. Sections 5–8 describe the properties of the radial velocities as well as their performance: accuracy, formal uncertainties, and median formal precision. Section 9 discusses the specific case of the high-velocity stars. Section 10 illustrates the properties of the radial velocities with specific objects: open clusters, globular clusters, and the Large Magellanic Cloud. Section 11 presents the performance of the variability indices. We conclude in Sect. 12.

## 2. Radial velocity spectrometer

This section briefly recalls the main characteristics of the RVS. For a full description of the instrument, we refer to Cropper et al. (2018).

The RVS is a spectrograph with a medium resolving power $R = \lambda/\Delta\lambda \sim 11\,500$ that works in the near-infrared $\lambda \in [845, 872]$ nm. The dispersion is oriented parallel to the scan direction (hereafter referred to as the along-scan direction). The RVS is illuminated by the two *Gaia* telescopes, which are imaged on the same block of 12 CCDs (three along-scan times four across-scan), located at the end of the focal plane. As a consequence, each time a star is observed (hereafter referred to as a transit), three spectra are recorded, that is, one per CCD along-scan. The exposure time is 4.42 s per CCD, or 13.2 s per transit.

*Gaia* scans the sky continuously, and the RVS records about eight transits per star per year on average. We note, however, that the individual number of transits is a strong function of the location on the celestial sphere (see Sect. 5.2) and that the effective number of transits that is used to derive the radial velocities is reduced by about 25% by the combination of the dead time (see Sect. 3.8) and the processing filters (see Sect. 4).

The satellite is not operated in pointing mode, but spins at a constant speed. It makes one full rotation every 6 h. The CCDs therefore do not record static images, but work in time-delay integration mode (TDI), that is, the charges are continuously transferred from CCD line to CCD line (and they are read continuously when they reach the read-out register), following the motion of the sources as they cross the fields of view.

The specificity of the RVS, which is pivotal in recording a very large number of spectra, is that it is an integral field spectrograph. It disperses all the light entering its two fields of view. Rectangular windows are selected around the sources of interest, stored in the on-board memory, and transferred during contact with the ground stations. The windows were initially 1260 pixels along-scan by 10 pixels across-can. In June 2015, the along-scan dimension was extended to 1296 pixels, while the across-scan dimension remained at 10 pixels. This increased the number of pixels outside the RVS bandwidth, which contributes to the calibration and correction of the background light. Overall, the configuration change had little impact on the accuracy of the radial velocity per transit, so that data collected before and after June 2015 can be combined without weighting. For stars brighter than $G_{RVS}$ = 7 mag, the full two-dimensional windows (called window class 0, or WC0) are transmitted to the ground segment. For the fainter stars, the across-scan dimension is collapsed at CCD level, and one-dimensional windows (window class 1, or WC1) are transferred. The pixels outside the windows are flushed, that is, they are clocked through the readout register, but are not read. The maximum number of windows that can be read and stored at any one time is limited to 72 per CCD (and fewer when stars brighter than $G_{RVS}$ = 7 mag are observed, as these stars use 10 resources each out of the available 72).

The RVS has no optomechanical device to select specific sources, such as slits or fibers, and it disperses all the light entering its two fields of view. As a consequence, spectra of very close sources will overlap. For stars fainter than $G_{RVS}$ = 7 mag, this generally results in the truncation of the windows containing the spectra. Over the area where the windows conflict, fewer than 10 pixels are assigned to each window. In many cases, this produces non-rectangular windows. A detailed description of the on-board window conflict resolution strategy is provided in Seabroke et al. (in prep.).

## 3. Spectroscopic pipeline

The core of the *Gaia* DR3 spectroscopic pipeline is similar to the pipeline operated for *Gaia* DR2 and described in Sartoretti et al. (2018). However, many new functionalities were added to improve the quality of the measurements and produce the new spectroscopic products that are published in *Gaia* DR3, that is, the radial velocities in the magnitude range $G_{RVS} \in [12, 14]$ mag, the hot star radial velocities (Blomme et al. 2023), the rotational broadening (Frémat et al. 2023), the $G_{RVS}$ magnitudes (Sartoretti et al. 2023), and the spectra (Seabroke et al., in prep.). After a brief overview of the *Gaia* DR3 spectroscopic pipeline (Sect. 3.1) and a presentation of the different estimates of $G_{RVS}$ (Sect. 3.2), the other parts of this section summarise the novelties implemented for the new release (with an emphasis on

those that are relevant for the derivation of the radial velocities; Sects. 3.3–3.7) and present the main aspects of the operations (Sect. 3.8). The on-line documentation provides a more thorough description of the *Gaia* DR3 pipeline (Sartoretti et al. 2022).

## 3.1. Overview

The *Gaia* DR3 spectroscopic pipeline is made of two technical and four scientific workflows. The two technical workflows, SourceInit and EpochInit, are in charge of preparing the data for the downstream workflows. In particular, SourceInit is tasked to gather, when available, the atmospheric parameters (effective temperature, surface gravity, and metallicity) of the sources that will be processed. At this stage, the atmospheric parameters can have two origins. They may come from an internal compilation of ground-based catalogues, or from the processing of the *Gaia* XP (i.e. low-resolution spectra collected by the blue and red spectrophotometers, Gaia Collaboration 2016) and RVS spectra performed by the General Stellar Parametrizer from photometry (GSP-Phot; Andrae et al. 2023) and from spectroscopy (GSP-Spec; Recio-Blanco et al. 2023). Each set of atmospheric parameters is later used in the spectroscopic pipeline to select the synthetic spectrum that is used as a template to derive the radial velocity (see Sect. 3.6).

The tasks of the four scientific workflows (i.e. straylight, calibration, FullExtraction, and STAMTA) are described below. The straylight workflow (Sect. 3.3) measures the background light level. The calibration workflow (Sect. 3.4) selects, reduces, and cleans the sources that are suitable for the self-calibration of the RVS and calibrates the following characteristics of the instrument: the wavelength scale, the along-scan line spread function (LSF) profile, the across-scan LSF profile, the across-scan location of the spectra, and the $G_{RVS}$ zeropoint. The FullExtraction workflow (Sect. 3.5) reduces and cleans the raw spectra to produce the calibrated spectra. For each raw spectrum, this includes the subtraction of the bias and bias non-uniformity (Hambly et al. 2018), the flagging of the saturated samples, the multiplication by the CCD gain, the subtraction of the dark current, the subtraction of the background light, the estimation of the flux lost outside of the window, the flagging of the spectra that overlap with cosmetic defects, the flagging of the spectra that have a bright neighbour, the detection and removal of the cosmic rays, the collapse of the two-dimensional windows (assigned on-board to stars brighter than $G_{RVS} = 7$ mag), the deblending of the spectra contained in overlapping windows, the transformation from pixel to wavelength, the measurement of the $G_{RVS}$ magnitude from RVS spectra, the division by the filter response, the normalisation of the fluxes, the detection and flagging of the emission lines and specific features (discontinuities or steep slope), and the determination of the atmospheric parameters (if unavailable in SourceInit). The STAMTA workflow (Sect. 3.6) processes the calibrated spectra to extract astrophysical information such as the radial velocity or the broadening velocity. It works source per source and is made of two parts: the single-transit analysis (STA), which analyses the data transit per transit, and the multiple-transit analysis (MTA), which combines and uses the transits recorded for each source together.

## 3.2. $G_{RVS}$ magnitudes

Several estimates of the $G_{RVS}$ magnitude are used in the spectroscopic pipelines and are referred to in the present paper: the

on-board $G_{RVS}$ ($G_{RVS}^{on-board}$), the external $G_{RVS}$ ($G_{RVS}^{ext}$), and the internal $G_{RVS}$ (grvs_mag).

The on-board $G_{RVS}$ is estimated by the *Gaia* on-board software prior to the observation by the RVS. It is either based on the signal in two specific samples in the red photometer or derived from the *G* magnitude. This magnitude estimate is used on board for the windowing and sampling decisions. It is transmitted to the ground together with the other data collected by the satellite.

The external $G_{RVS}$ is derived from *Gaia* DR2 $G$ and $G_{RP}$ magnitudes (Evans et al. 2018; Riello et al. 2018), when available, following Eqs. (2) and (3) from Gaia Collaboration (2018). About 2.5% of the stars processed by the spectroscopic pipeline lacked a $G$ and/or $G_{RP}$ measurements. In this case, the on-board $G_{RVS}^{on-board}$ is used instead. It should be noted that the definition of $G_{RVS}^{ext}$ in *Gaia* DR3 differs from the one adopted in *Gaia* DR2 (see Sartoretti et al. 2018; Katz et al. 2019). The latter used the $G_{RVS}$ from the Initial *Gaia* Source List (IGSL; Smart & Nicastro 2014).

The internal $G_{RVS}$ is the median of the $G_{RVS}$ magnitudes evaluated at each transit by measuring the flux contained in the RVS spectra in the wavelength range [846, 870] nm. The internal magnitudes are published in *Gaia* DR3 in the field grvs_mag, contained in the gaia_source table (Sartoretti et al. 2023).

The selection of the stars entering the different workflows is based on the $G_{RVS}^{ext}$ magnitudes. In particular, only stars with $G_{RVS}^{ext} \leq 14$ mag are processed by the STAMTA workflow, thus setting the limit for the derivation and publication of the radial velocities in *Gaia* DR3. The internal $G_{RVS}$ magnitudes are calculated within the STAMTA workflow. This was too late for grvs_mag to play the role assigned to the external magnitude. However, the internal $G_{RVS}$ is used to define the threshold between the two methods that calculate the combined radial velocity (see Sect. 3.6). In Sects. 6–8, the accuracy, formal uncertainties, and median formal precisions are presented as a function of grvs_mag.

## 3.3. Straylight workflow

The *Gaia* commissioning revealed that the level of background light was higher than expected prior to launch. The reason is that straylight from the Sun and from the brightest stars is diffracted at the edge of the Sun shield, entering the satellite through the apertures of the telescopes and reflected via different optical paths up to the focal plane.

In *Gaia* DR2, a single calibration of the background was performed, based on the data from the first 28 days of the mission. It produced a set of three maps (one for each group of four RVS CCDs aligned across-scan) of the background light as a function of the satellite rotation phase and of the across-scan location in the focal plane. These maps were used to correct the full 22-month dataset. This calibration alone could not account for the temporal variations of the background and led to under- and over-corrections of the fluxes. In *Gaia* DR3, the background maps are produced every 30 h of mission time, using 72 h of data (i.e. 21 h before and 21 h after).

The first beneficiary of the temporal sampling is the measurement of the internal $G_{RVS}$ magnitudes, thus based on better corrected estimates of the stellar fluxes. The combined radial velocities also benefit from the improved background calibration. In the *Gaia* DR2 and *Gaia* DR3 pipelines, a spectrum from which an over-estimated sky background is subtracted and whose total flux becomes negative (which could occur for the faintest stars) is rejected from the processing. Therefore, the improvement of

the precision of the calibration of the background light increases the number of spectra that are combined to derive the *Gaia* DR3 radial velocities.

### 3.4. Calibration workflow

In the *Gaia* DR2 pipeline, two static models of the along-scan LSF were used. The first was calibrated using reference spectra collected during the first 28 days of the mission and was applicable up until the first decontamination on 23 September 2014 (see Sect. 3.8). The second model was based on pre-launch measurements and was used for the remaining 20 months of data. In the *Gaia* DR3 pipeline, the along-scan LSF calibration has been upgraded to better monitor the temporal variations of the instrumental profile. As described in Sartoretti et al. (2018, 2022), an along-scan LSF is represented mathematically as the weighted sum of fixed profiles, also called basis functions (Lindegren 2009). The purpose of the along-scan LSF calibration is to constrain the weights. In *Gaia* DR3, the 34 months are split into ten periods, whose boundaries correspond to discontinuities in the RVS instrument calibrations. In each period, the weights are modelled with either constant or linear functions, depending on which is most appropriate. The templates used in the STAMTA workflow to measure the transit radial velocities (see Sect. 3.6) are produced by convolving synthetic spectra with the along-scan LSF. The upgrade of this calibration improves the match between the templates and the observed spectra and consequently improves the radial velocities.

In the *Gaia* DR3 pipeline, two new characteristics of the RVS instrument are also calibrated: the across-scan LSF profile, and the across-scan location of the spectra in the focal plane. Both pieces of information are required to model and disentangle the fluxes of the spectra contained in conflicting windows (see Sect. 3.5).

### 3.5. FullExtraction workflow

It happens that RVS spectra overlap, either because the sources are very close on the sky or because two sources are observed each by a different telescope (we recall that *Gaia* has two telescopes), but their images end up close in the focal plane by mischance. If the sources are brighter than the RVS limiting magnitude $G_{RVS} = 16.2$ mag and if the limit of window resources is not exceeded (see Sect. 2), a window is allocated to each. The windows then contain a mix of the source fluxes. Moreover, if the sources are fainter than $G_{RVS} = 7$ mag, the windows are usually truncated in the across-scan dimension. The truncated windows can be thinner but still rectangular if they share the same along-scan boundaries, but most of the time, they present an L-shape or a more complex geometry (when more than two sources are involved). In the *Gaia* DR2 pipeline, only rectangular windows were processed. All the others were discarded. In the *Gaia* DR3 pipeline, a new functionality, deblending, has been implemented to handle truncated windows. It uses the mix of fluxes contained in the windows together with the calibrations of the across-scan LSF profile and of the across-scan location of the spectra to reconstruct the spectrum of each source separately. The deblended spectra represent slightly more than 25% (about 540 million out of 2 billion) of the spectra processed by the STAMTA workflow. Of the 33 812 183 stars for which a combined radial velocity is published in *Gaia* DR3, about 96% have at least one deblended transit. The on-board window han-

dling strategy and the deblending method are described in detail in Seabroke et al. (in prep.).

### 3.6. STAMTA workflow

The STAMTA workflow is the last stage of the pipeline that in particular measures the combined radial velocities. This section summarises the different steps of the derivation of the radial velocities and presents two new *Gaia* DR3 functionalities that select the templates of hot stars and derives the combined radial velocities of the faint stars, respectively. The STAMTA workflow is described in more detail in the on-line documentation (Sartoretti et al. 2022).

#### 3.6.1. Single-transit analysis

The STAMTA workflow consists of two parts. The first part, the single-transit analysis (STA), processes the calibrated spectra per source and per transit to measure the epoch radial velocities and the epoch rotational broadenings (the latter are provided by a new functionality implemented in *Gaia* DR3; Frémat et al. 2023). The first task performed by STA is to detect the double-line spectra, which are analysed by a dedicated method (Damerdji et al., in prep.). A radial velocity value is derived for each component. They are then used within the *Gaia* non-single star processing (Damerdji et al., in prep.), but they are not published in *Gaia* DR3. The bulk of the spectra are single line. They are analysed by three different modules, which are all based on the comparison between a reference template shifted step by step in radial velocity and the three observed spectra collected per transit. Two of the modules quantify the match between the template and the observation with cross-correlation functions (one in direct space and the other in Fourier space), while the third relies on a chi-square minimum-distance method (David et al. 2014; Sartoretti et al. 2018). The epoch radial velocity is calculated as the median of the estimates provided by the three methods. The epoch radial velocities are not published in *Gaia* DR3, except for a selected sample of slightly fewer than 2000 Cepheids and RR-Lyrae (contained in the table `vari_epoch_radial_velocity`). The publication of the radial velocity time series is planned for *Gaia* DR4.

The choice of the template does influence the quality of the epoch radial velocities. A significant mismatch between the template and the observed spectra can degrade the precision, and to a greater extent, the accuracy. The template mismatch prevented the publication of the radial velocities of hot stars ($T_{eff} \geq 7000$ K) in *Gaia* DR2. The first step to select a template is to assign atmospheric parameters (effective temperature, surface gravity, and metallicity) to the source that is processed. The atmospheric parameters can have different origins, and the first origin that is available in the following list is used: (1) an internal compilation of ground-based catalogues (see Sartoretti et al. 2022, for the full list of catalogues), (2) an early run of the *Gaia* General Stellar Parametrizer from Spectroscopy (GSP-spec; Recio-Blanco et al. 2023), and (3) an early run of the *Gaia* General Stellar Parametrizer from Photometry (GSP-phot; Andrae et al. 2023). If none of these is available, the module determineAP is called (as part of the FullExtraction workflow). It handles bright and faint stars differently. For stars with $G_{RVS}^{ext} \leq 12$ mag, it cross-correlates a limited set of 28 synthetic spectra (convolved by the along-scan LSF profile) with the observed spectra and returns the parameters of the synthetic spectrum producing the tallest peak. One set of

parameters is derived per transit, and the set with the most frequent occurrence is assigned to the star, in order to use the same template for all transits from the same source. Stars with $G_{\mathrm{RVS}}^{\mathrm{ext}} > 12$ mag are too noisy, and they are assigned default parameters ($T_{\mathrm{eff}} = 5500$ K, $\log g = 4.5$ and [Fe/H] = 0.0 dex) by determineAP. When the atmospheric parameters are set, the synthetic spectrum with the closest parameters (following Eq. (11) of Sartoretti et al. 2018) from a library of 6772 spectra is chosen as template. Although this selection is appropriate for cool stars, it is affected by the same template mismatch issue as *Gaia* DR2 was for hot stars. For *Gaia* DR3, a new module, reDetermineApHotStars, was implemented to refine the selection of their templates. It is called for stars with a first determination of the template $T_{\mathrm{eff}} \geq 6500$ K (if the atmospheric parameters are from the compilation of catalogues) or 7000 K otherwise. It compares the observed spectra to the full subset of the library of synthetic spectra with $T_{\mathrm{eff}} \geq 6500$ K source by source. The parameters of the best-matched synthetic spectrum (in the chi-square sense) supersede those of the first determination. The module reDetermineApHotStars is called for stars brighter than $G_{\mathrm{RVS}}^{\mathrm{ext}} = 12$ mag, but not for fainter stars, whose spectra are too noisy. The design and performance of reDetermineApHotStars is the subject of a companion paper (Blomme et al. 2023). The parameters of the selected templates are stored in the fields `rv_template_teff`, `rv_template_logg` and `rv_template_fe_h` in the `gaia_source` table. The origin of the atmospheric parameters that are used to choose the template is encoded in the field `rv_atm_param_origin`.

### 3.6.2. Multiple-transit analysis

The second part of the STAMTA workflow, the multiple-transit analysis (MTA), works source by source, using the time series to compute the combined radial velocities, the `grvs_mag` magnitudes (Sartoretti et al. 2023), the combined spectra (Seabroke et al., in prep.), and variability indices. The combined radial velocity of stars brighter than `grvs_mag` = 12 mag is calculated in the same way as in *Gaia* DR2 (Sartoretti et al. 2018; Katz et al. 2019), that is, as the median of the epoch radial velocities (expressed in the Solar System barycentre reference frame). The calculation of the formal uncertainty on the measurement of the combined radial velocity is very similar as well, with only a minor change in the constant term,

$$\epsilon_{V_{\mathrm{R}}} = \left[ \left( \sqrt{\frac{\pi}{2N}} \sigma_{V_{\mathrm{R}}^{\mathrm{t}}} \right)^2 + (0.113)^2 \right]^{0.5}, \qquad (1)$$

where $N$ is the number of transits used to derive the median radial velocity, $\sigma_{V_{\mathrm{R}}^{\mathrm{t}}} = \sqrt{\frac{1}{N-1} \sum_{i=1}^{N} (V_{\mathrm{R}}^{\mathrm{t}}(i) - \overline{V_{\mathrm{R}}^{\mathrm{t}}})^2}$ is the standard deviation of the epoch radial velocity time series, $V_{\mathrm{R}}^{\mathrm{t}}(i)$ is the $i$th transit radial velocity within the time series, and $\overline{V_{\mathrm{R}}^{\mathrm{t}}}$ is the mean of the time series. The constant term, 0.113 km s$^{-1}$, is meant to take the wavelength calibration errors and similar sources of uncertainties into account. It was estimated using a subset of the catalogue of radial velocity stable stars of Soubiran et al. (2018b).

Beyond `grvs_mag` = 12 mag, the epoch radial velocities are not considered reliable enough to derive the combined radial velocities. A new method has therefore been implemented in the *Gaia* DR3 pipeline to process the stars in the magnitude range `grvs_mag` ∈ [12, 14] mag. Source by source, (i) it loads the Fourier space cross-correlation functions derived in STA for all the transits of that source, (ii) it shifts them by the barycentric correction, (iii) it averages them, and (iv) it measures the combined radial velocity as the location of the maximum of the averaged cross-correlation function. The formal uncertainty is derived from the sharpness of the summit of the cross-correlation function and implements the formula proposed by Zucker (2003) in his Sect. 2.3, quadratically summed with the same constant term as in Eq. (1),

$$\epsilon_{V_{\mathrm{R}}} = \left[ \left( \frac{C^2 - 1}{\mathrm{rv\_nb\_transits} \times N \times C'' \times C} \right) + (0.113)^2 \right]^{0.5}, \qquad (2)$$

where $N$ is the number of pixels in the spectrum, $C''$ is the value of the second derivative of the cross-correlation function estimated at its summit, and $C$ is the maximum value of the cross-correlation function.

In the magnitude range `grvs_mag` ∈ [11, 12] mag, just before the transition between the two methods, the radial velocity formal uncertainties show an extended tail (see Fig. 4 in Babusiaux et al. 2023). It is sparsely populated and does not produce any significant discontinuity on the radial velocity precision, which is estimated using the median of the formal uncertainties (see Sect. 8). However, the threshold at `grvs_mag` = 12 mag might be slightly lowered in *Gaia* DR4.

The combined radial velocities and their formal uncertainties are stored in the fields `radial_velocity` and `radial_velocity_error` in the `gaia_source` table, respectively. The method is provided by the field `rv_method_used`: 1 for the median of the epoch radial velocities (hereafter referred to as the modelling method), and 2 for the combination of the cross-correlation functions (hereafter referred to as the robust method).

### 3.7. Variability indices

Except for a very small number of variable stars, the epoch radial velocities are not published in *Gaia* DR3, but they will be in *Gaia* DR4. However, *Gaia* DR3 contains two variability indices, based on the properties of the time series.

`rv_chisq_pvalue` is the *p*-value for the constancy of the radial velocity time series. It ranges from zero for a low-probability constancy to one for the high probability (i.e. the scatter of the epoch radial velocities is entirely due to measurement errors and not to intrinsic properties of the source).

`rv_renormalised_gof` is calculated as the F2-value (see Vol. 1, Sect. 2.1 of ESA 1997) of the renormalised unit-weight error of the radial velocity time series. For constant stars, it should follow a normal distribution of standard deviation equal to one. Variable stars will exhibit high values (compared to unity).

These two variability indices require precise measurements of the epoch velocities. For this reason, they are only calculated down to magnitude `grvs_mag` = 12 mag. `rv_chisq_pvalue` is also restricted to stars with `rv_nb_transits` ≥ 3 and `rv_renormalised_gof` to stars with `grvs_mag` ≥ 5.5 mag and `rv_template_teff` < 14 500 K. Moreover, the reliability of the two indices increases with the number of measurements. It is therefore recommended to use them for stars that have been observed at least ten times (`rv_nb_transits` ≥ 10). Finally, both indices rely on the comparison of the scatter of the epoch radial velocities to the epoch radial velocity formal uncertainties. The latter are less precise for `rv_template_teff` < 3900 and > 8000 K. The variability indices will be more reliable in between these two values.

The two indices agree well and can be combined in a single variability criterion. The following conservative criterion can be used to identify variable stars: `rv_nb_transits` ≥ 10 & `rv_template_teff` ∈ [3900, 8000] & `rv_chisq_pvalue` ≤ 0.01 & `rv_renormalised_gof` > 4. The performances of this criterion are assessed in Sect. 11.

In addition to the two variability indices, *Gaia* DR3 also provides the measurement of the peak- to-peak amplitude of the radial velocity time series (after filtering of the outliers): `rv_amplitude_robust`. The three fields are stored in the table `gaia_source`.

### 3.8. Operations

*Gaia* DR3 is based on the data collected during the first 34 months of the nominal mission, that is, from 25 July 2014 to 28 May 2017. During this period, several on-board operations were performed. The main operations were the three decontaminations, during which specific parts of the payload were reheated to sublimate the remnants of water ice (23 September 2014, 3 June 2015, and 22 August 2016) and the two refocus operations (24 October 2014 and 3 August 2015). These operations, as well as some other minor events, either prevented the acquisition of the data or degraded the data, which were then excluded from the processing. In total, 92.2% of the 34 months were ingested in the spectroscopic pipeline, while the remaining 7.8% were either unavailable or considered unfit for processing[1].

The data were processed by the 2500 cores of the Hadoop cluster of the Centre National d'Études Spatiales (CNES) in Toulouse, France. The 2.8 billion spectra of the stars brighter than $G_{\rm RVS}^{\rm ext} = 14$ mag were ingested in the spectroscopic pipeline (plus approximately 12 billion spectra of fainter stars, potentially needed by the deblending module and used for that purpose only). Approximately 855 million were filtered out within the FullExt workflow (see Sect. 4.2), and the remaining 2 billion were processed by the STAMTA workflow. The full processing required about 3 million CPU hours, or 120 days in real time. It occupied approximately 300 TB of disc space for the input, intermediate, and output data. It produced 37 499 608 combined radial velocities as well as broadening velocities (Frémat et al. 2023), `grvs_mag` magnitudes (Sartoretti et al. 2023), and combined spectra (Seabroke et al., in prep.).

## 4. Filtering unreliable data

Quality checks were carried out throughout the production of the radial velocity catalogue: first on the input data, then during processing, and finally, on the catalogue itself during the validation phase. The spectra, transits, or sources that failed the tests were discarded. The filters are described in the sections below.

We note that the *Gaia* DR3 filtering is deliberately not informed by the previous validation of *Gaia* DR2. In *Gaia* DR3, the spectra, transits, or sources that were excluded from *Gaia* DR2 were all re-examined. In *Gaia* DR4, it is foreseen to proceed similarly. Moreover, some filters should be removed and replaced by probabilistic quality indices, thus allowing the users to optimise their selection according to their science case.

---

[1] The list of gaps in the spectroscopic data processing is available on the ESA-*Gaia* website: https://www.cosmos.esa.int/web/gaia/dr3-data-gaps

### 4.1. Input data

The first series of filters was applied to the input data before they were transmitted to the scientific processing. We describe them below.

Bad-data intervals. The transits recorded during the 7.8% of the time considered as unfit for processing (see Sect. 3.8) were removed.

Low-quality astrometry. The astrometry is used together with the calibration of the satellite attitude to derive the coordinates of the source in the field of view (the along- and across-scan field angles $\eta$ and $\zeta$) for each pixel in a spectrum when the pixel crosses the CCD central line (also called fiducial line). The field angles are used within the FullExtraction workflow to apply the wavelength calibration. Accurate radial velocities require an accurate wavelength calibration and therefore accurate astrometry. The sources were therefore removed in the following cases: (i) missing or not converged astrometric global iterative solution (AGIS; Lindegren et al. 2021) coordinates, (ii) AGIS flagged the source as duplicated, (iii) AGIS used fewer than five observations, (iv) the source `astrometric_excess_noise` is higher than 20 mas, or (v) the source `astrometric_sigma5d_max` > 100 mas.

Low-quality field angles. The RVS dispersion is oriented along-scan. As a consequence, an error on the along-scan field angle $\eta$ propagates linearly to the wavelength zeropoint. Transits with uncertainties on $\eta$ higher than 200 mas (corresponding to about 29 km s$^{-1}$) were removed.

### 4.2. Processing

We describe the filters that were applied in the course of the processing below.

Large number of saturated pixels. Spectra containing more than 40 saturated pixels were removed.

Negative total flux. Spectra with a negative total flux (after bias, bias non-uniformity, and background subtraction) were removed.

High background. The background was subtracted from the spectra in the FullExtraction workflow. Unfortunately, the additional photon noise that is added by this cannot be corrected for. Spectra with a background (i) higher than 100 e$^-$ pixel$^{-1}$ s$^{-1}$ or (ii) higher than 40 e$^-$ pixel$^{-1}$ s$^{-1}$ and an uncertainty on the background calibration higher than 0.4 e$^-$ pixel$^{-1}$ s$^{-1}$ were considered to be significantly contaminated and were removed.

CCD cosmetic defects. Spectra containing a CCD column that was affected by a cosmetic defect were removed.

Neighbour without a window. It may happen that a star has a bright neighbour that does not have a window. In this case, the new deblending functionality (Sect. 3.5, Seabroke et al., in prep.) is not triggered because it requires the (truncated) windows of both sources. To mitigate the risk of contamination, an area corresponding to about 2500 pixels along-scan by 20 pixels across-scan was monitored around each spectrum. If at least one star without an RVS window and a magnitude smaller than that of the observation plus three (i.e. $G_{\rm RVS}^{\rm ext}$(neighbour) < $G_{\rm RVS}^{\rm ext}$(observation) + 3) was found in this area, the spectrum was considered as significantly contaminated and was removed.

Large number of cosmic rays. Spectra containing 100 or more pixels that were hit by cosmic rays were removed.

Non-deblended truncated windows. Two main reasons can prevent the deblending module from working (see Seabroke et al., in prep.): either one of the truncated windows is missing, or the information contained in the windows is insufficient

to reconstruct the spectra reliably (this can in particular happen when the separation between the sources is very small and the spectra are almost colocated). Spectra contained in truncated windows that could not be successfully processed by the deblending module were removed.

Emission-line stars. The spectroscopic pipeline includes a module for detecting emission-line stars. However, it does not have templates that reproduce these stars. The resulting template mismatch can produce systematic errors on the radial velocity of several hundred kilometres per second. As a consequence, the combined radial velocities of about 25 000 sources, with 40% or more transits flagged as emission lines, were not computed.

Corrupted spectra. The module detecting the emission-line stars also performs sanity checks on the spectra. Those presenting instrumental or numerical artefacts (e.g. a sudden discontinuity) were removed.

Of the 2.8 billion spectra processed in *Gaia* DR3, about 855 million were removed within the FullExtraction workflow, and 2 billion were transmitted to the STAMTA workflow. The two main causes for which spectra were rejected were when they could not be deblended (~540 million spectra) and when they had a bright neighbour without a window (~135 million spectra).

### 4.3. Validation

The STAMTA workflow produced 37 499 608 combined radial velocities. These were examined during the validation phase, and a last set of filters was applied. About 3.7 million measurements were removed, while 33 812 183 combined radial velocities successfully passed the quality checks and are published in *Gaia* DR3. The filters are presented in the sections below.

#### 4.3.1. Stellar and galactic properties

The *Gaia* DR3 spectroscopic pipeline processed all the spectra recorded during the first 34 months of the mission down to $G_{\rm RVS}^{\rm ext} \leq 14$ mag, without any selection on stellar type or colour indices. However, some objects require specific analyses that are not or not yet implemented in the spectroscopic pipeline or are implemented in other *Gaia* processing pipelines. Some selections were therefore performed a posteriori.

Double-line spectroscopic binaries. The combined radial velocity does not provide a good estimate of the systemic velocity of double-line spectroscopic binaries, and it is not suitable for describing the variations in the velocities of the two components. Approximately 40 000 sources for which 10% transits or more were flagged as double-line were considered SB2 candidates, and their combined radial velocities were discarded. The epoch radial velocities of these sources were transmitted to the *Gaia* non-single star group, who processed them. They publish their orbital elements in *Gaia* DR3 (Damerdji et al., in prep.).

Emission-line stars. The pipeline filtered stars for which 40% transits or more were flagged as emission-lines. In validation, this threshold was lowered to 30%. A few more emission-line stars that were identified visually were also discarded. In total, another 3000 combined radial velocities were removed. The library of templates is scheduled to be updated with emission-line spectra in *Gaia* DR4.

Cool stars. The validations showed that the accuracy and precision of the cool stars down to `rv_template_teff` = 3100 K were of good enough quality to be published in *Gaia* DR3. The

combined radial velocities of about 243 000 stars cooler than 3100 K were removed.

Hot stars. The module reDetermineApHotStars allows refining the selection of the hot star template (see Sect. 3.6.1 and Blomme et al. 2023). It was used to process sources down $G_{\rm RVS}^{\rm ext} \leq 12$ mag, but not the fainter stars because the transit spectra then become too noisy. As a consequence, faint hot stars are affected by the same template mismatch issue as in *Gaia* DR2 (Katz et al. 2019), which prevents their publication. The combined radial velocities of approximately 1.7 million stars with `grvs_mag` > 12 and `rv_template_teff` ≥ 7000 K were removed.

The module reDetermineApHotStars allows mitigating the template mismatch of the bright stars for `rv_template_teff` in the range [6500, 14 500] K (Blomme et al. 2023). Beyond this temperature, significant radial velocity systematics persist; this will require further improvements in *Gaia* DR4. For *Gaia* DR3, the combined radial velocities of approximately 66 000 stars with `grvs_mag` ≤ 12 and `rv_template_teff` > 14 500 K were removed.

Several *Gaia* pipelines are interdependent: the output of one is the input of the other. As a result, they often cannot operate in parallel, but are time shifted. Toward the end of the validation phase, the *Gaia* Extended Stellar Parameterizer – Hot Stars (ESP-HS; Creevey et al. 2023) completed its final run and own validation. The effective temperatures derived by ESP-HS were compared to the template temperatures. It revealed a group of 20 470 stars with cool templates (`rv_template_teff` ≤ 7000 K), but effective temperatures estimated by ESP-HS that were higher than or equal to 7500 K. In this temperature range, a template mismatch can produce very significant radial velocity systematics. For safety, their combined radial velocities were removed.

Extra-galactic sources. The spectroscopic pipeline processes all spectra assuming the source is a star. Although the limiting magnitude of $G_{\rm RVS}^{\rm ext} \leq 14$ mag is bright for galaxies and quasars, a few may have made their way into the processing. No suitable treatment is provided for these objects, and their combined radial velocities would be erroneous. Two groups of (potential) extra-galactic objects were identified and removed. The first consists of 112 sources with `phot_bp_rp_excess_factor` > 13 and `bp_rp` ∈ [1.2, 1.8] mag, which was interpreted as an extra-galactic signature. The second group contains nine sources that were individually confirmed as galaxies or quasars. We note that 4027 sources in the `qso_candidates` table and 160 in the `galaxy_candidates` table also possess a combined radial velocity in the *Gaia* DR3 catalogue because it has not been possible to confirm or refute their extra-galactic nature during the validation phase. These sources are briefly discussed in Gaia Collaboration (2023a). The classification of the sources, including the extra-galactic sources, is presented in Delchambre et al. (2023) and in Rimoldini et al. (2023) for the variable sources.

#### 4.3.2. Noisy data

To reach $G_{\rm RVS}^{\rm ext} = 14$ mag, the spectroscopic pipeline processed spectra with a very low signal-to-noise ratio (S/N), sometimes below $S/N = 1$ per pixel (after combining the information from all the transits). In the very low S/N regime, spurious secondary cross-correlation peaks can exceed the (true) main peak, leading to an erroneous radial velocity measurement. Several filters were applied to mitigate this problem.

Faint `grvs_mag` magnitudes. The stars processed in *Gaia* DR3 were selected on the basis of their external $G_{\rm RVS}^{\rm ext}$ magnitudes because the internal `grvs_mag` magnitudes, computed by the STAMTA workflow, were not yet available. During the validation phase, the two measurements were compared and agreed well overall (Sartoretti et al. 2023). However, some stars exhibited an internal magnitude that was significantly fainter than 14. In order to achieve a relatively sharp cut-off in magnitudes (both external and internal) for *Gaia* DR3, stars fainter than `grvs_mag` = 14.5 mag were excluded from the release. The stars whose transits were all deblended constitute a special case. Their mean flux (recorded in the wavelength range [846, 870] nm) is measured, but their internal magnitude is not derived. An alternative but equivalent filter was applied to these stars. Those with a mean flux lower than 525 e⁻ s⁻¹ were discarded. In total, approximately 21 000 combined radial velocities were removed.

Suspicious cross-correlation functions. The noise in the spectrum propagates to the cross-correlation function and modifies its morphology. This information can be used to detect spurious radial velocities. The *Gaia* DR3 spectroscopic pipeline measures several characteristics of the combined cross-correlation function, such as maximum value, full width at half maximum, kurtosis, skewness, ratio, and the distance between the two highest peaks and a few more. These quantities are not published in the release, but were available for the validation phase. These parameters (complemented by the combined radial velocity formal uncertainty) were used, together with a set of APOGEE DR14 data (Abolfathi et al. 2018), to train a model to identify the spurious combined radial velocities. First, the training set was divided between valid and invalid radial velocities, based on the residuals: *Gaia* DR3 minus APOGEE. Then, thresholds were defined for the different parameters that allowed us to separate the valid and invalid radial velocities. For *Gaia* DR3, the model was trained in the traditional way by visualising the data in various data spaces. For *Gaia* DR4, machine-learning approaches are explored. The combined radial velocities of the stars with `grvs_mag` ≥ 12 mag are measured from the combined cross-correlation function (see Sect. 3.6.2). The model was therefore applied over the same magnitude range. About 2.9 million stars were flagged as invalid, and their combined radial velocities were removed. In a second step, still during the validation phase, the model was improved with two more quantities to characterise the cross-correlation function. The application of the upgraded model required the offline regeneration and characterisation of the combined cross-correlation functions. The offline processing capabilities were more limited than those of the nominal processing, therefore, the application of the model was restricted to stars whose absolute value of the combined radial velocity was higher than or equal to 300 km s⁻¹ (but without a selection on `grvs_mag`). This offline run led to the removal of about 34 500 additional combined radial velocities.

Low S/Ns. The filter on the morphology of the cross-correlation function removed 2.9 million stars and was effective in removing spurious measurements. However, at very low S/N, the estimated rate of invalid radial velocities (estimated from the shape of the radial velocity distribution, see Sect. 9) was still high to very high: between 5 and 10% for $S/N \in [1.5, 2.0]$ and several dozen percent for $S/N \in [0.0, 0.5]$. As a consequence, the combined radial velocities of the ~270 000 sources with S/N `rv_expected_sig_to_noise` < 2, were removed.

Large formal uncertainties. As described above, the formal uncertainties on the measurements of the combined radial velocities were used together with the characteristics of the cross-correlation functions to identify spurious velocities in

two data sets: stars with `grvs_mag` ≥ 12 mag and those with $|V_{\rm R}| \geq 300$ km s⁻¹. The stars whose combined radial velocity formal uncertainty was larger than 40 km s⁻¹ were flagged as invalid. For consistency, the same filter was applied to the stars whose cross-correlation function was not examined. This filter removed approximately 65 800 additional combined radial velocities. This criterion not only discards spurious measurements, but also large-amplitude binaries and variables. Therefore, the epoch radial velocities of these stars were transmitted to the *Gaia* non-single star and variability analysis groups for analysis and publication of the genuine large-amplitude sources (Gosset et al., in prep.; Clementini et al. 2023).

Large scatter of the epoch radial velocities. The combined radial velocities of about 2500 stars brighter than `grvs_mag` ≤ 12 mag whose scatter of the epoch radial velocities was larger than 577 km s⁻¹ were removed. This conservative threshold corresponds to the standard deviation of a uniform distribution over the range [−1000, +1000] km s⁻¹.

Inconsistent results from different methods. In the nominal run, combined radial velocities of faint stars (`grvs_mag` ≥ 12 mag) are derived using a single method based on the analysis of the average Fourier space cross-correlation functions (see Sect. 3.6.2). However, test and validation runs were conducted with complementary methods using (i) the average direct space cross-correlation function, (ii) the average chi-square minimum-distance function, and (iii) the combined epoch spectra. The bulk of the stars showed a satisfactory agreement between the different estimators. However, the combined radial velocities of about 48 500 stars with a large discrepancy between the nominal run method and the other methods were removed.

### 4.3.3. Contaminated data

Because the RVS has no optomechanical device to select specific sources and disperses all the light entering its two fields of view, neighbouring stars can contaminate each others. If the overlapping spectra are close enough, they are either handled by the deblending module (if all windows are available; see Sect. 3.5) or are filtered out (if some windows are missing; see Sect. 4.2). However, when a source is bright enough, it can contaminate its neighbours at larger distances than the area considered by the nominal processing. Several filters were used to identify and remove the invalid radial velocities resulting from the contamination by these stars.

Stars with bright neighbours. When in a given window, the flux of a neighbour exceeds the flux of the object targetted, the epoch radial velocity measured is usually the one of the contaminant. Moreover, this radial velocity is shifted by the offset between the wavelength reference frames of the two spectra (contaminated and contaminant), which, to first order, is proportional to the along-scan distance between the sources: $\Delta$frames $\sim 145 \times d_{\rm AL}$ (where the offset $\Delta$frames is expressed in km s⁻¹ and the along-scan distance $d_{\rm AL}$ is in arcsec). This can produce very high spurious values, as in the case of star *Gaia* DR2 5932173855446728064 (Boubert et al. 2019). For along-scan separations larger than about 6.9 arcsec, the offset between the wavelength reference frames exceeds the radial velocity measurement interval of [−1000, +1000] km s⁻¹ and the epoch radial velocity becomes pseudo-random. The contamination happens at transit level. However, if the sources are either very close, or if they are observed repeatedly in the same configuration (i.e. similar along-scan separations), or if the contaminating flux largely exceeds the observation flux, the combined radial

velocity can be spoiled. Only a few stars in the Milky Way have high radial velocities (positive or negative), and even a small number of outliers can produce a significant contamination rate. Therefore, particular attention was paid to stars with $|V_R| > 200 \, \text{km s}^{-1}$. There are 17 697 stars with a *Gaia* DR3 combined radial velocity in this range and one or more neighbours with a brighter $G$-band magnitude within a radius of 10 arcsec. Figure 1 shows the difference in $G$-band magnitude between these stars and their neighbours ($\Delta G = G_{\text{star}} - G_{\text{neigh}}$) as a function of their separations on the sky. The colour code provides the absolute value of the *Gaia* DR3 combined radial velocity of the stars. The stars mainly fall into two groups: one group with a small difference in magnitude, and the other with a larger difference. In the top group, the absolute value of the combined radial velocity correlates with the distance between the star and its neighbour. As described above, this behaviour is precisely expected when the flux recorded in a window is dominated by a contaminant. The lower group does not show significant signs of correlation, which indicates that the measured velocities are not spoiled by contaminants. The separation between the two groups was modelled by a straight line ($\Delta G = 0.6 \times d + 1.0$) that was manually adjusted. It is represented by the dashed grey line in Fig. 1. Of the 1624 stars located on or above this limit, 1623 were removed. The star *Gaia* DR3 4657994321463473792, which sits almost on the dividing line and has very consistent velocities in APOGEE DR17 (Abdurro'uf et al. 2022) and in *Gaia* DR3 (273.5 km s$^{-1}$ and 273.3 km s$^{-1}$, respectively), was kept. As we recalled in Sect. 2, the two *Gaia* fields of view are imaged on the same focal plane. As a result, the bright contaminant and the contaminated star can originate from the two different fields of view, which are separated by 106.5° (Gaia Collaboration 2016). The filter described above, which checks for the presence of brighter sources within 10 arcsec of each target, cannot detect contaminants from the other field of view. In addition to the first group of 1623 stars, another 25 contaminated stars were identified with an alternative criterion and were removed. Finally, using the binary catalogue of El-Badry et al. (2021), the *Gaia* catalogue validation group also identified 57 stars separated by less than 1.6 arcsec from their companion and showing differences in radial velocities larger than 500 km s$^{-1}$ (Babusiaux et al. 2023). Their combined radial velocities were removed.

Contaminated spectra. The RVS bandpass filter has relatively steep wings. They are trimmed within the FullExtraction workflow, which keeps only the wavelength range [846, 870] nm. However, on rare occasions, the combined spectra produced by the STAMTA workflow (Seabroke et al., in prep.) still exhibit a wing. This is caused by a bright contaminant, which is shifted in the dispersion direction (i.e. along-scan) with respect to the contaminated spectra. On the detector, the wing of the bright contaminant overlaps with the area corresponding to the wavelength range [846, 870] nm of the contaminated spectra. The combined radial velocities of 18 stars presenting this feature were removed.

### 4.3.4. Other filters and caveat

Two more filters were applied during the validation phase. They are described below.

Inconsistent location of the calcium triplet lines. The combined radial velocities of 172 stars that were inconsistent with the location of the calcium triplet lines in their combined spectrum were removed. The reason for this inconsistency is not yet understood.

High Velocity Stars (HVS) with inconsistent bibliographic measurements. The combined radial velocities of 14 HVS
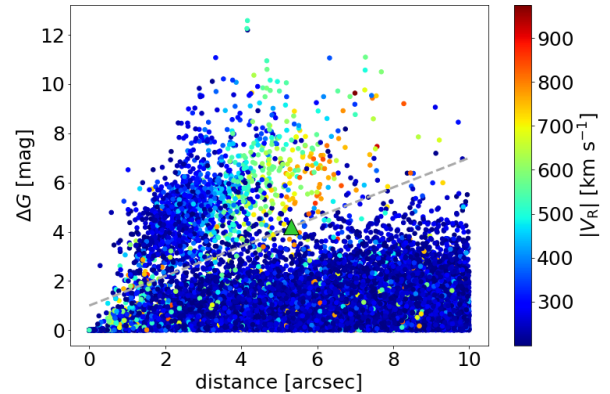


**Fig. 1.** Differences in $G$-band magnitude between the stars and their neighbours as a function of their separations on the sky for the 17 697 sources with $|V_R| > 200 \, \text{km s}^{-1}$ and one or more neighbours with a brighter $G$-band magnitude within a radius of 10 arcsec. The colour code provides the absolute value of the *Gaia* DR3 combined radial velocities for the star. The dashed grey line shows the separation between the spurious and valid velocity measurements. The green triangle shows the location of star *Gaia* DR3 4657994321463473792, which was kept in the release even though it is located slightly above the dividing line (see text).

(defined as stars with $|V_R| \geqq 500 \, \text{km s}^{-1}$), which were strongly discrepant with the literature, were removed. A different approach will probably be used for future data releases. Rather than removing radial velocity measurements, a flag or source list may be provided for some objects or object types to report significant disagreements between *Gaia* and the literature.

Caveat about white dwarfs. The spectroscopic pipeline has no appropriate template for white dwarfs. The resulting mismatch between the observed spectra and the templates can produce large systematic radial velocity errors. The spectroscopic pipeline did not have access to information to identify these objects. Consequently, their radial velocities were not removed from *Gaia* DR3, but they should be considered with great caution.

## 5. *Gaia* DR3 radial velocity catalogue

### 5.1. Content overview

*Gaia* DR3 contains the combined radial velocities of 33 812 183 stars. The dataset extends to two magnitudes fainter than *Gaia* DR2 (Katz et al. 2019) and *Gaia* EDR3 (Seabroke et al. 2021), that is, down to $G_{\text{RVS}}^{\text{ext}} = 14$ mag. The temperature interval was also expanded from `rv_template_teff` $\in$ [3600, 6750] K in *Gaia* DR2 to `rv_template_teff` $\in$ [3100, 14 500] K for the bright stars ($G_{\text{RVS}}^{\text{ext}} \leq 12$ mag) and [3100, 6750] K for the fainter stars. The database also contains complementary information, such as the formal uncertainty on the radial velocity, the parameters of the template, and the variability indices. The list of products from the spectroscopic pipeline published in *Gaia* DR3 is provided in Tables B.1 and B.2.

Figure 2 (top) shows the distribution on the sky of the stars with a combined radial velocity in *Gaia* DR3. As expected, the bulk of the dataset belongs to the Milky Way. However, the *Gaia* DR3 radial velocity catalogue also includes stars from satellite galaxies, such as the Large Magellanic Cloud (LMC; $l = 280.5°$, $b = -32.9°$) and the Small Magellanic Cloud (SMC; $l = 302.8°$, $b = -44.3°$, see Sect. 10.3), which are well visible in the lower right corner of the image, or Sagittarius (less clearly visible in
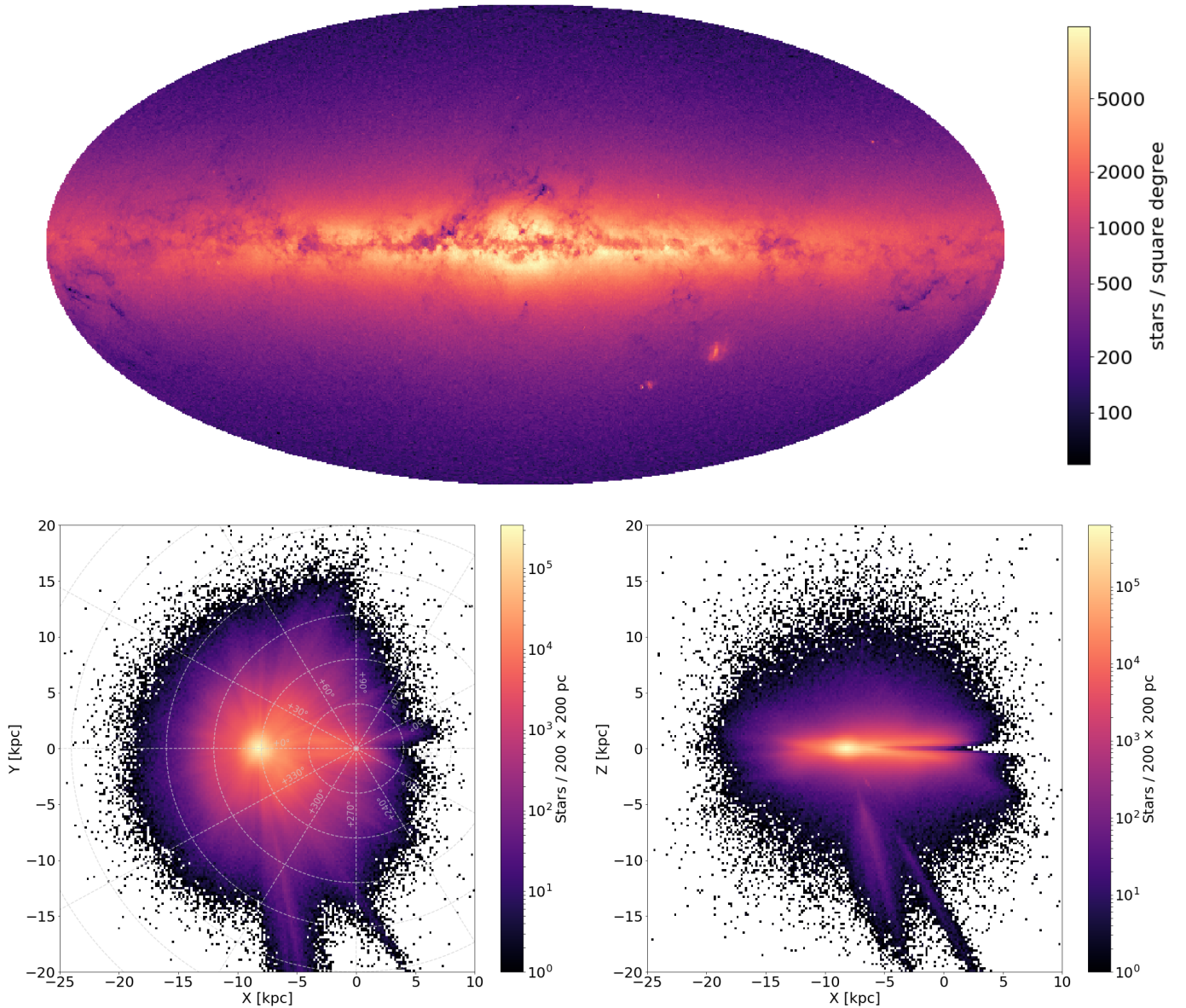
**Fig. 2.** Spatial distributions of the *Gaia* DR3 radial velocities. *Top*: sky distribution of the 33 812 183 stars whose combined radial velocity is published in *Gaia* DR3. The image uses a Mollweide projection in Galactic coordinates $(l, b)$. The Galactic centre is at the centre of the figure, and the Galactic longitudes increase to the left. The sampling of the map is approximately 0.2 square degree (healpix level 7). *Bottom left*: face-on view of a sub-sample of 29.4 million stars (see text) in galactocentric Cartesian coordinates $(X, Y)$. The Galactic centre is located at $X = Y = 0$ kpc, and the Sun is at $X = -8.277$ kpc (GRAVITY Collaboration 2022) and $Y = 0$ kpc. In this image, the Milky Way is seen from the Galactic north pole and rotates clockwise. The sampling is $200 \times 200$ parsec$^2$. *Bottom right*: edge-on view of the same sub-sample in galactocentric Cartesian coordinates $(X, Z)$. The Galactic centre is located at $X = Z = 0$ kpc, and the Sun is at $X = -8.277$ kpc and $Z = 20.8$ pc (Bennett & Bovy 2019). The $Z$-axis is oriented positive towards the Galactic north pole. The sampling is $200 \times 200$ parsec$^2$.

this image, but see Sect. 5.4). Moreover, a significant fraction of the known globular clusters (GC) are also part of *Gaia* DR3. The number of velocity measurements per GC ranges from a few to more than one thousand (see Sect. 10.2).

In *Gaia* DR2, the $G_{\rm RVS}^{\rm ext}$ magnitudes used to select the stars mainly came from the initial *Gaia* source list (IGSL; Smart & Nicastro 2014). They were calculated from several catalogues, mostly GSC2.3 (Lasker et al. 2008), *Tycho*-2 (Høg et al. 2000), and SDSS (Strauss et al. 2002). The heterogeneity of the input photometry produced small offsets in the resulting $G_{\rm RVS}^{\rm ext}$, and some spatial fluctuations in the GSC2.3 $B_J$ and $R_F$ magnitudes (in particular in the overlapping areas of the photometric plates) were propagated to the calculated magnitudes.

This produced small spatial variations in the limiting magnitude of the *Gaia* DR2 spectroscopic catalogue, and the footprints of the GSC2.3 and SDSS were visible in the radial velocity sky map (Katz et al. 2019; Rybizki et al. 2021). In *Gaia* DR3, the $G_{\rm RVS}^{\rm ext}$ magnitudes were mainly calculated from $G$ and $G_{\rm RP}$ magnitudes (Sect. 3.2). The top part of Fig. 2 shows that the *Gaia* DR3 sky map exhibits significantly fewer selection artefacts.

Figure 2 (bottom) presents the distributions of the stars in the galactocentric Cartesian $XY$ (left) and $XZ$ planes (right). The maps show a sub-sample of 29.4 million stars after sources with an astrometric renormalised unit weight error `ruwe` $\geq 1.4$ or with `duplicated_source` set to `True` were removed. The
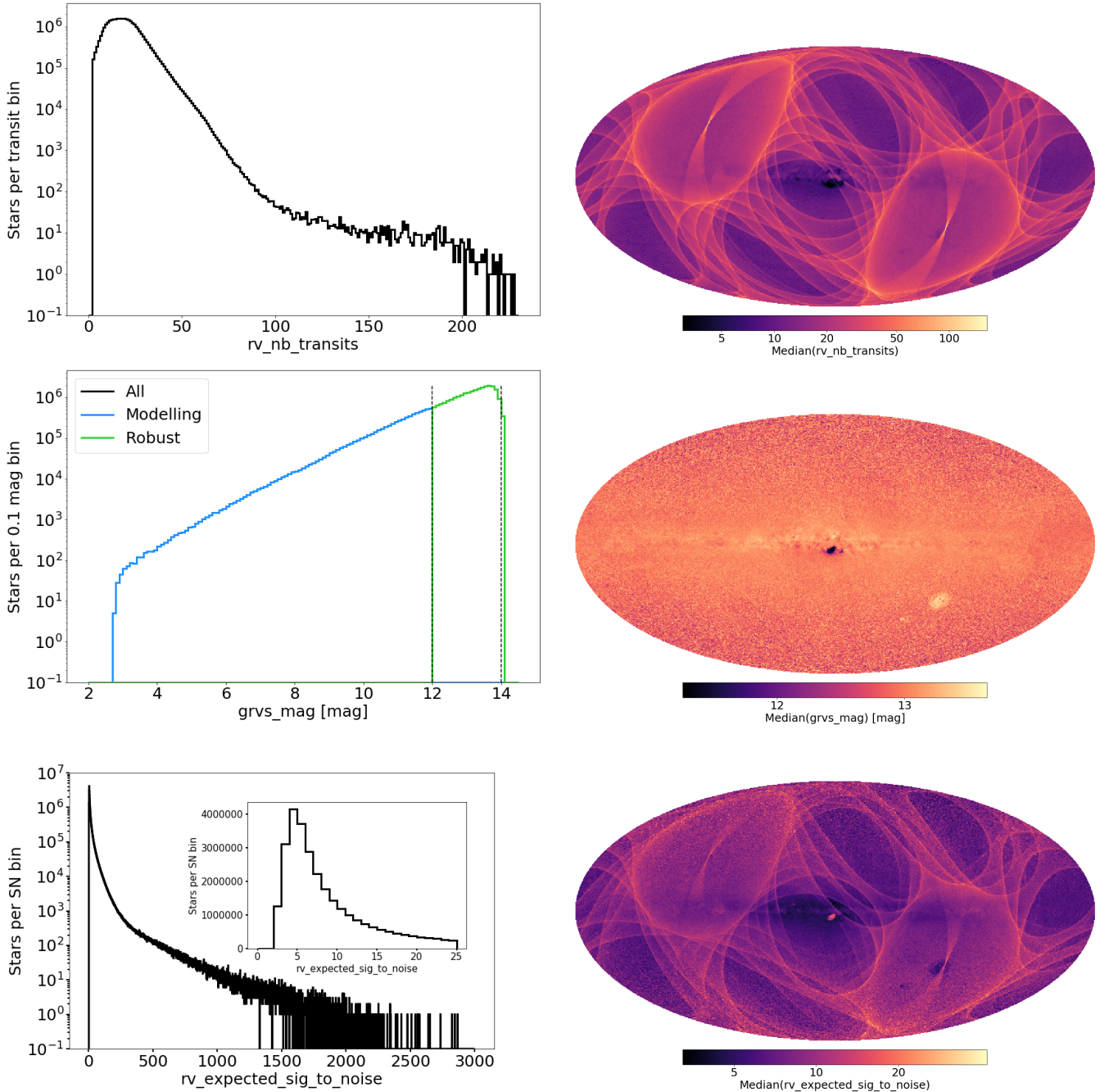
**Fig. 3.** Distributions of the numbers of transits (rv_nb_transits, *top*), grvs_mag magnitudes (*middle*), and S/N (rv_expected_sig_to_noise, *bottom*) of the stars whose combined radial velocity is published in *Gaia* DR3. In the *left column*, the distributions are presented in the form of histograms. The *right column* presents the sky maps of the median values of these three quantities. The maps use Mollweide projections in Galactic coordinates (*l, b*). The Galactic centre is at the centre of the images, and the Galactic longitudes increase to the left. The sampling of the maps is approximately 0.2 square degree (healpix level 7).

coordinates were calculated with the Bayesian photogeometric distances from Bailer-Jones et al. (2021). The face-on view shows that the radial velocity catalogue now samples a significant part of the Milky Way disc. It extends a few kiloparsecs beyond the Galactic centre and therefore allows us to probe the kinematic of the bar (Gaia Collaboration 2023b). Vertically, the catalogue encompasses the thin and thick discs and part of the inner halo, up to about 10−15 kpc. The two elongated features at negative *Y* and negative *Z* are LMC and SMC stars, whose distances are under-estimated (see the discussion in Bailer-Jones et al. 2021).

### 5.2. Transits, magnitudes, and signal-to-noise ratios

Figure 3 shows the distribution of the numbers of transits, `rv_nb_transits` (top), `grvs_mag` magnitudes (middle), and S/N, `rv_expected_sig_to_noise` (bottom) of the stars whose combined radial velocity is published in *Gaia* DR3. In the left column, the distributions are presented in the form of histograms. The right column presents the sky maps of the median values of these three quantities.

The number of transits ranges from 2 (minimum number for the pipeline to calculate the combined radial velocity) to 227,

with a median number of 18. As shown by the sky map, over most of the celestial sphere, the number of transits is driven by the satellite scan law. In particular, during the first month of the nominal mission, the satellite was operated in ecliptic pole scanning law (EPSL) mode. During this period, the northern and southern ecliptic poles were monitored by each telescope every 6 h, collecting large numbers of observations of the stars in these two areas. The number of transits drops sharply in the densest regions (the less strongly extincted ones) of the bulge and disc. Three effects combine to produce this rapid decrease. First, from approximately 36 000 stars per square degree, the maximum number of windows that can be allocated is reached (see Sect. 2), so that some spectra are not recorded. Then, it happens that when the satellite scans the Galactic plane for several days, the on-board memory is saturated and the lowest priority data (usually the faintest stars) must be erased before they can be transmitted to the ground. Finally, in these dense regions, a very large fraction of the spectra are blended, and if the deblending cannot be performed (either because a window is missing or because the sources are too close; see Seabroke et al., in prep.), the radial velocity is not derived. We note that these effects occur at transit level, and therefore, they primarily impact the number of transits, but can also affect the completeness.

The `grvs_mag` magnitude is not calculated for the stars with deblended transits only. The number of stars with a `grvs_mag` magnitude published in *Gaia* DR3 is 32 276 087 (Sartoretti et al. 2023), slightly lower than the number of radial velocities. The bright limit of the velocity catalogue is `grvs_mag = 2.76` mag and results from the saturation of the RVS spectra. The magnitude of the faintest star is `grvs_mag = 14.1` mag. The transition between the two methods used to calculate the combined radial velocities (modelling in blue and robust in green) occurs at `grvs_mag = 12` mag. The sky map of the median `grvs_mag` magnitudes is relatively smooth and homogeneous over much of the celestial sphere. It is fainter in the direction of the Magellanic Clouds because of the excess of intrinsically fainter sources belonging to the two galaxies. Conversely, the median magnitude is brighter in the densest regions of the bulge because the windowing scheme and the on-board storage-deletion schemes both favour the bright stars.

The lower limit of the S/N was set at 2 during the validation phase, in order to minimise the contamination by spurious radial velocity values (see Sect. 4.3.2). The highest S/N is 2868 (for star *Gaia* DR3 413828761929696256, `grvs_mag = 3.82` mag and 62 transits). The distribution is very asymmetric and contains only a few high values. The median of the distribution is 7.8. The map shows that over most of the sky, the median S/N is driven by the scanning law (through the number of transits). However, the median S/N are lower in the direction of the Magellanic Clouds and higher in the densest regions of the bulge because the median `grvs_mag` magnitudes are fainter and brighter there, respectively.

## 5.3. Completeness

In this section, the completeness is estimated with respect to the *Gaia* catalogue as a whole. That is, as the ratio of the number of stars with a radial velocity to the total number of stars in the catalogue, either per bin of magnitude (Fig. 4, top) or per healpix cell (Fig. 4, bottom).

Figure 4 (top) compares the completeness of the *Gaia* DR3 (black curve) and *Gaia* EDR3 (red curve) radial velocity catalogues as a function of *G* magnitude. The longer time baseline and the upgrade of the *Gaia* DR3 pipeline have improved the
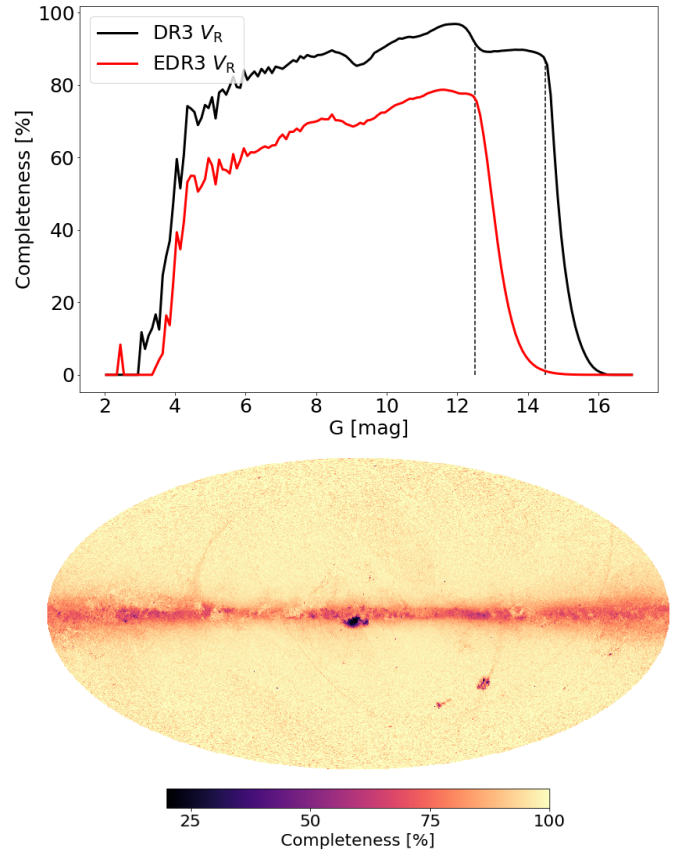


**Fig. 4.** *Top*: completeness of the *Gaia* DR3 (black curve) and *Gaia* EDR3 (red curve) combined radial velocity catalogues as a function of *G* magnitude. Two dashed vertical lines are drawn at *G* = 12.5 and *G* = 14.5 mag, corresponding to the respective drops in completeness of each of the catalogues. *Bottom*: sky map of the completeness with respect to the *Gaia* DR3 catalogue (restricted to stars with *G* ≤ 14.5 mag). The image uses a Mollweide projection in Galactic coordinates (*l*, *b*). The Galactic centre is at the centre of the image, and the Galactic longitudes increase to the left. The sampling of the map is approximately 0.2 square degree (healpix level 7).

completeness with respect to the previous release. In addition to the offset between the two curves, they exhibit similar trends with an increase in completeness over the entire range, from *G* ∼ 4 to ∼12 mag. The sharp drop below *G* ∼ 4 mag is caused by the saturation of the spectra. On the other side, the *Gaia* DR3 completeness drops around *G* = 14.5 mag, which is two magnitudes fainter than *Gaia* EDR3 (consistent with the extension of the processing limit from $G_{RVS}^{ext}$ = 12 to $G_{RVS}^{ext}$ = 14). We note that the majority of the stars have fainter *G* than $G_{RVS}$ magnitudes (an un-reddened G2V star has $G - G_{RVS} \sim 0.65$ mag), which explains that the drop occurs at *G* ∼ 14.5 mag. The moderate decrease around *G* ∼ 8.5 mag is produced by the transition from 2D windows (WC0) to 1D windows (WC1). The first are never truncated, but the second can be. The 1D windows therefore suffer from a higher rejection rate, corresponding to the cases where the spectra cannot be deblended (see Sect. 4.2). Between *G* ∼ 12 and 12.5 mag, the completeness decreases slightly and then stays roughly flat up to 14.5 mag. The decrease is the result of filters applied in validation, in particular, the removal of (i) the hot stars with `grvs_mag > 12` mag and `rv_template_teff ≥ 7000` K (see Sect. 4.3.1), and of (ii) the stars with spurious cross-correlation functions (see Sect. 4.3.2).
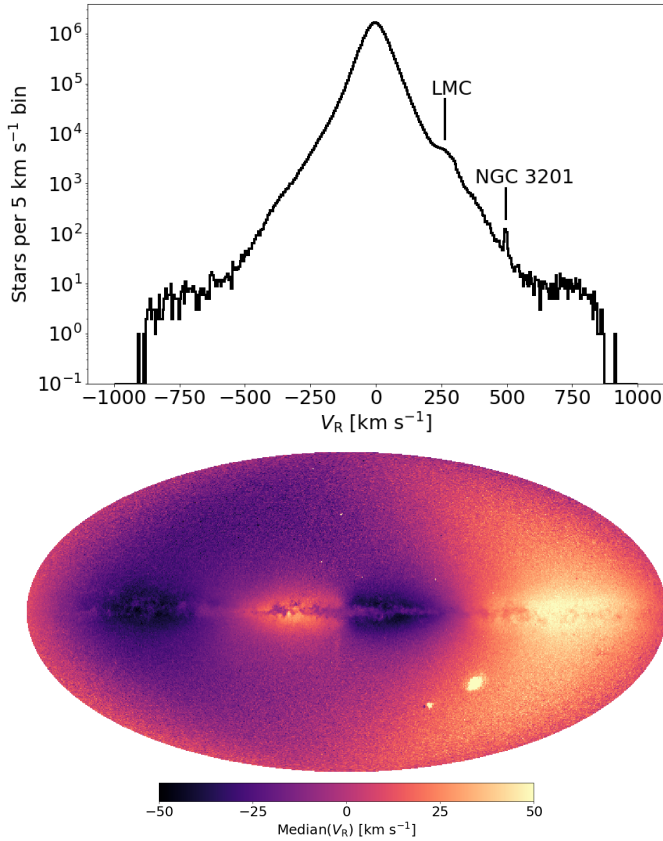
**Fig. 5.** *Top*: histogram of the 33 812 183 combined radial velocities. The sampling is $5\,\mathrm{km\,s^{-1}}$ per bin. *Bottom*: sky map of the median radial velocity. The image uses a Mollweide projection in Galactic coordinates $(l, b)$. The Galactic centre is at the centre of the image, and the Galactic longitudes increase to the left. The sampling of the maps is approximately 0.2 square degree (healpix level 7). The limits of the colour bar have been set at $-50$ and $+50\,\mathrm{km\,s^{-1}}$ in order to highlight the median velocity variations in the disc.

Figure 4 (bottom) shows the sky map of the completeness with respect to the *Gaia* DR3 catalogue (restricted to stars with $G \leq 14.5$ mag). The completeness varies inversely with stellar density. It is maximum outside the Galactic plane, decreases in the disc, and drops in the least extincted and therefore densest areas of the bulge.

### 5.4. Radial velocities

Figure 5 (top) shows the histogram of the 33 812 183 combined radial velocities. Most of the sources belongs to the Milky Way disc and are centred around $\sim 0\,\mathrm{km\,s^{-1}}$. Two specific objects stand out in the right wing of the distribution. On the one hand, the LMC appears as a bump around $+262\,\mathrm{km\,s^{-1}}$ (McConnachie 2012). On the other hand, the high-velocity GC NGC 3201 is visible as a spike around $+494\,\mathrm{km\,s^{-1}}$ (Baumgardt et al. 2019). The outer part of the wings of the distribution, beyond $|V_R| \gtrsim 500{-}600\,\mathrm{km\,s^{-1}}$, does flatten. This indicates that the proportion of spurious measurements remains significant in the very-high velocity regime. The specific case of the HVSs is discussed in Sect. 9.

Figure 5 (bottom) shows the map of the median radial velocities as a function of Galactic longitudes and latitudes. The rotation of the Galactic disc (projected along the lines of sight) is manifested by the alternation of bright areas (with positive median velocities) and dark areas (with negative median velocities). Several objects whose radial velocities differ from those of their close environment (and which are sufficiently populated to weigh on the median value) are visible by contrast. In addition to the LMC and SMC appearing as bright spots in the lower right corner of the image, the Sagittarius dwarf galaxy is visible as a faint quasi-vertical stripe below the Galactic centre. Several GC and compact objects appear as tiny dots in the image, such as 47 Tuc, the dark dot ($V_R = -17\,\mathrm{km\,s^{-1}}$, Baumgardt et al. 2019) just left of the SMC, or Omega Cen, a bright dot ($V_R = 234\,\mathrm{km\,s^{-1}}$, Baumgardt et al. 2019) at $l \sim 309°$ and $b \sim +15°$.

## 6. Accuracy

Formally, the accuracy is the systematic difference between the measured values and the true values. However, the true values, which would allow assessing the systematics in absolute terms, are not known. As a consequence, we assess the systematic differences in relative terms in this section by comparison to five ground-based catalogues: APOGEE DR17 (Abdurro'uf et al. 2022), GALAH DR3 (Buder et al. 2021; Zwitter et al. 2021), the *Gaia*-ESO Survey (GES) DR3 (see for the survey description, Gilmore et al. 2012; Randich et al. 2013), LAMOST DR7 (see for the survey and pipeline description, Zhao et al. 2012; Deng et al. 2012; Luo et al. 2015), and RAVE DR6 (Steinmetz et al. 2020b,a). Quality filters are applied before comparison. They are described in Appendix C.

The relative accuracy is estimated as the median of the radial velocity residuals: *Gaia* DR3 minus the ground-based catalogue. The boundaries of the 68.3% confidence interval on this estimator are calculated as

$$\epsilon_{\mathrm{acc}}^{\mathrm{low}} = \sqrt{\frac{\pi}{2N}}(\tilde{V}_R^{\mathrm{res}} - \mathrm{Per}(V_R^{\mathrm{res}}, 15.85)) \qquad (3)$$

$$\epsilon_{\mathrm{acc}}^{\mathrm{upp}} = \sqrt{\frac{\pi}{2N}}(\mathrm{Per}(V_R^{\mathrm{res}}, 84.15) - \tilde{V}_R^{\mathrm{res}}), \qquad (4)$$

where $N$, $\tilde{V}_R^{\mathrm{res}}$, $\mathrm{Per}(V_R^{\mathrm{res}}, 15.85)$, and $\mathrm{Per}(V_R^{\mathrm{res}}, 84.15)$ are the number of elements, the median, and the 15.85th and 84.15th percentiles of the distribution of radial velocity residuals, respectively.

### 6.1. Magnitude trend

In the *Gaia* DR2 catalogue, the radial velocities showed a systematic magnitude trend, starting around $G_{\mathrm{RVS}} \sim 9$ mag and reaching about $500\,\mathrm{m\,s^{-1}}$ at $G_{\mathrm{RVS}} \sim 11.75$ mag (Katz et al. 2019; Tsantaki et al. 2022). At the time of publication of *Gaia* DR2, the origin of the trend was not understood. Posterior tests showed that the amplitude of the bias decreases when the intensity of the background light increases. This strongly suggests that the trend is produced by traps in the CCD pixels. Traps can snare a part of the recorded signal and prevent it from propagating from CCD line to CCD line. After a while, the trapped photo-electrons are released. If this occurs fast enough for the spectrum to have moved only one or a few pixels, the released photo-electrons will skew the line profiles in the direction opposite to the propagation of the signal. In the RVS, the shorter wavelengths lead. Traps would therefore skew the lines toward longer wavelengths, mimicking a positive radial velocity shift. Pre-launch laboratory tests showed that the weaker the signal, the stronger the trapping effect. This would explain both that the intensity of the bias
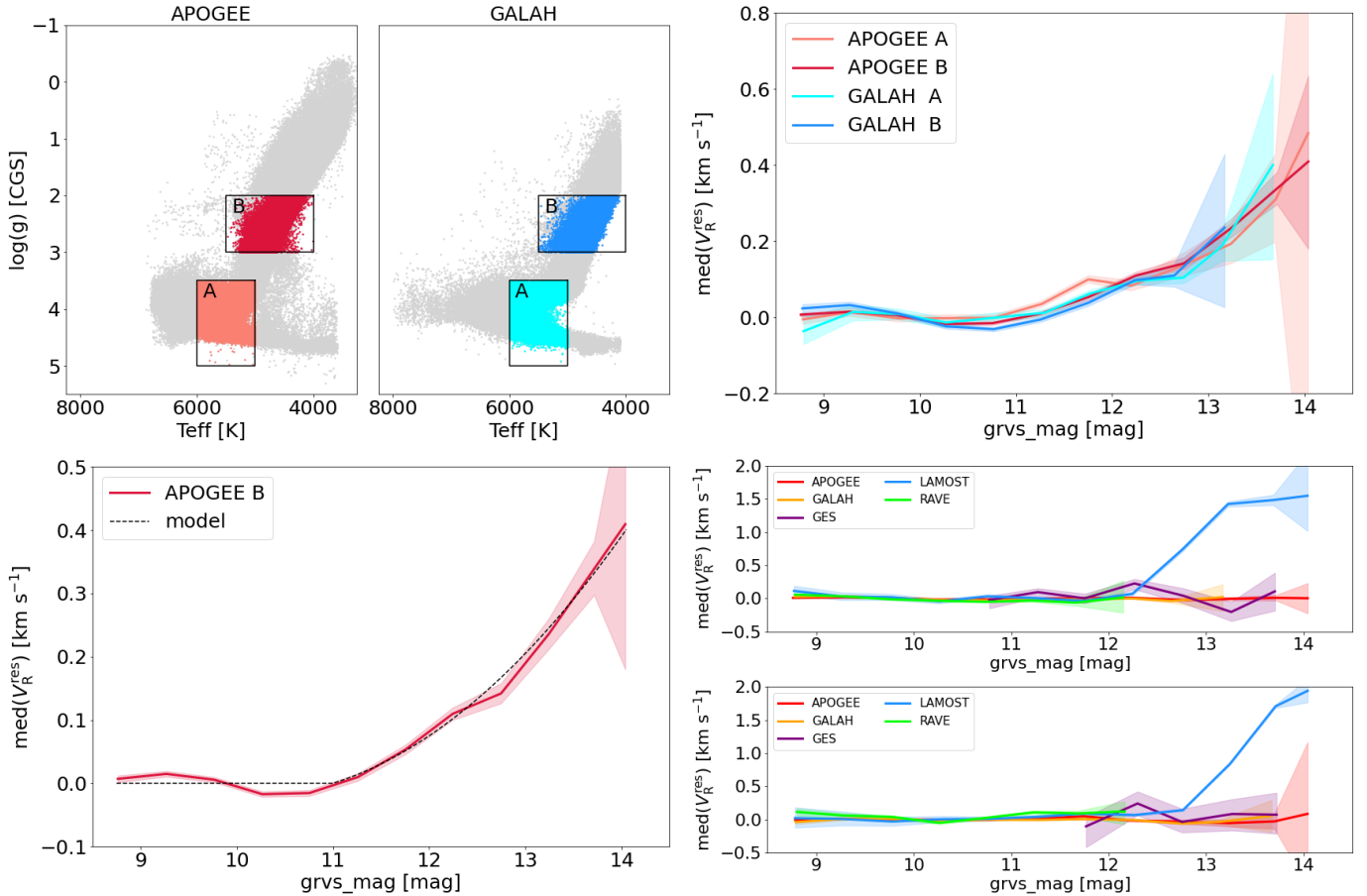
**Fig. 6.** *Top left*: Kiel diagrams of the APOGEE and GALAH catalogues. The groups of stars selected to assess the magnitude trend are shown in salmon and cyan (group A: dwarfs and turn-off stars) and red and blue (group B: giants). *Top right*: median residuals of the radial velocity (*Gaia* minus catalogue) as a function of grvs_mag magnitude for the four samples. *Bottom left*: radial velocity correction model (dashed line) over-plotted on the median residuals of the radial velocity of the APOGEE B sample (red curve). *Bottom right*: median residuals of the radial velocity as a function of grvs_mag magnitude after applying the radial velocity correction, with respect to the five reference catalogues APOGEE, GALAH, GES, LAMOST, and RAVE. The *upper panel* shows group B stars (giants), and the *lower panel* presents group A stars (dwarfs and turn-off stars). All curves are shifted vertically (see text) and therefore show relative trends. The 68.3% confidence interval on the measurements of the medians is represented as shaded areas.

increases with magnitude and that, in contrast, the background light reduces the effect. The tests did not show a significant time dependence of the trend, at least over the first 34 months of data. It is therefore likely that the majority of the traps were present from the start of the mission and that so far, only a few of them are the result of cosmic-ray damage.

Early in the preparation of *Gaia* DR3, the trend was modelled as a function of magnitude and background-light intensity. During processing, the model was used to correct the epoch radial velocities and the epoch cross-correlation functions before computing the combined radial velocities. In order to assess whether the calibration fully removed the magnitude trend or if a residual bias remained, we compared the *Gaia* DR3 velocities to those of the APOGEE and GALAH catalogues. Figure 6 (top left) shows the Kiel diagrams of the two catalogues. In each, two groups are selected, one made of dwarf turn-off stars (group A: salmon in APOGEE and cyan in GALAH), and the other made of red giants and clump stars (group B: red in APOGEE and blue in GALAH). The two samples were restricted to the metallicity range [Fe/H] ∈ [−0.5, 0.5] dex to avoid mixing potential magnitude and metallicity trends. Figure 6 (top right) presents the median of the radial velocity residuals (*Gaia* minus catalogue) as a function of grvs_mag magnitude for the four sam-

ples. The curves are adjusted vertically, so that their positions coincide on the bright side, with the aim to compensate for possible offsets between dwarfs and giants or between APOGEE and GALAH. The adjustment was made by subtracting the median value of the radial velocity residuals measured in the magnitude range grvs_mag ∈ [8.5, 10.5] mag. The four curves exhibit a very similar trend: quasi-flat for grvs_mag ≤ 11 mag, and then increasing to reach about 400 m s⁻¹ at grvs_mag = 14 mag. There is therefore a residual trend, and the consistency between the four samples of different origins and properties indicates that this trend is in the *Gaia* DR3 combined radial velocities.

The sample APOGEE B contains the largest number of sources (129 598 giants) and also has the most precise median trend. It is therefore used to model the radial velocity bias by fitting a second-order polynomial to the median trend. The model is applicable to stars fainter than grvs_mag = 11 mag. Figure 6 (bottom left) shows the model (dashed line) over-plotted on the median residuals of the radial velocities of the APOGEE B sample (red curve). The combined radial velocities published in *Gaia* DR3 are not corrected for the magnitude trend. To mitigate it, we therefore recommend to subtract from *Gaia* DR3 radial_velocity (for stars with
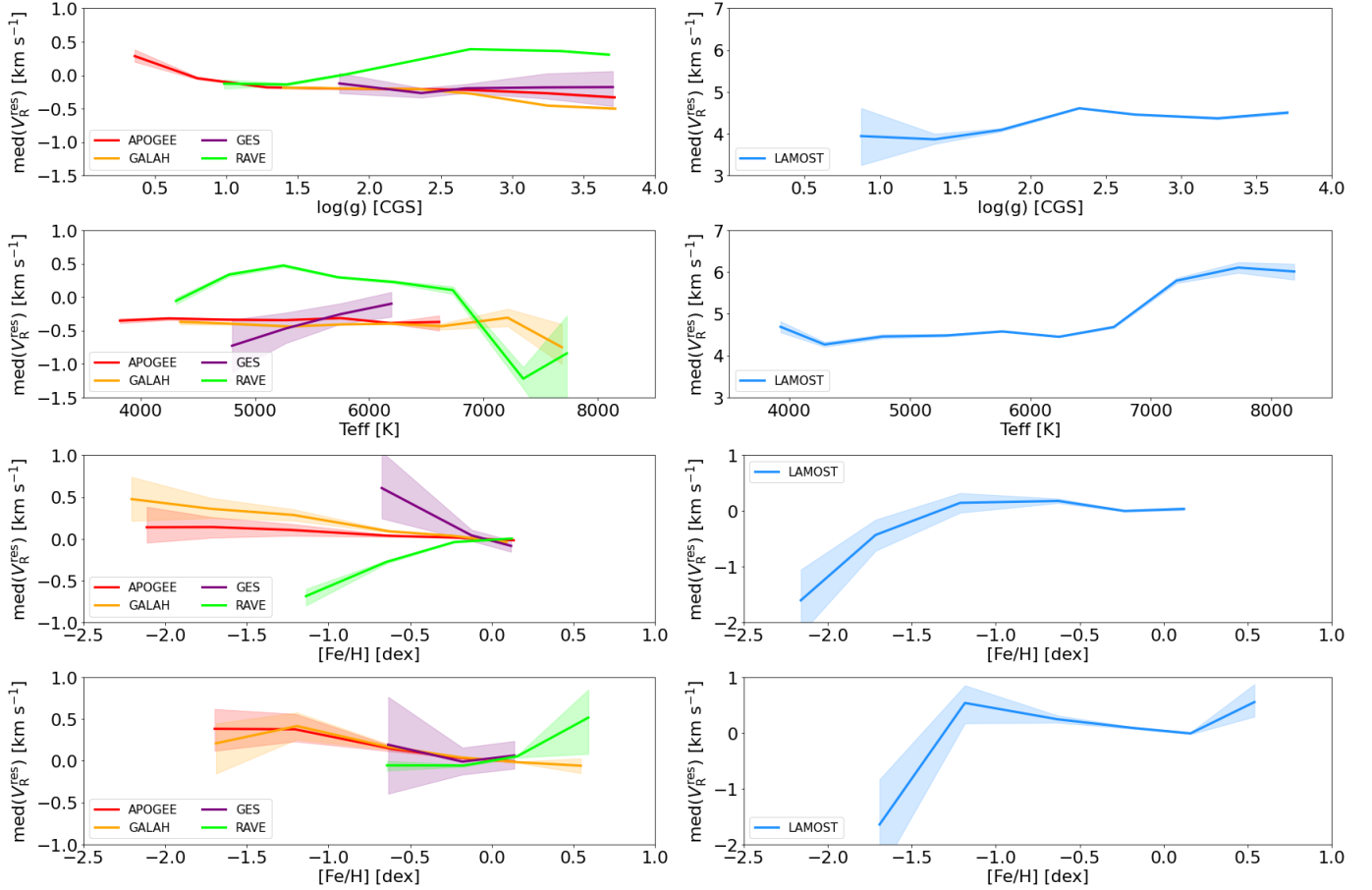
**Fig. 7.** *From top to bottom, row 1*: median residuals of the radial velocity as a function of surface gravity for samples of metal-rich giants. *Row 2*: median residuals of the radial velocity as a function of effective temperature for samples of metal-rich main sequence stars. *Rows 3 and 4*: median residuals of the radial velocity as a function of metallicity for samples of giants and main-sequence stars, respectively. The metallicity trends are presented relative to solar metallicity (see text). The 68.3% confidence interval on the measurements of the medians is represented as shaded areas.

`rv_template_teff` < 8500 K)

$$\begin{aligned} \text{grvs\_mag} &< 11 : V_R^{corr} = 0 \, \text{km s}^{-1} \\ \text{grvs\_mag} &\geq 11 : V_R^{corr} = 0.02755 \times \text{grvs\_mag}^2 \\ &\quad - 0.55863 \times \text{grvs\_mag} \\ &\quad + 2.81129 \, \text{km s}^{-1} \end{aligned}. \quad (5)$$

The hot stars also exhibit a magnitude trend, but it is quite different from that of the cooler stars. For the stars with a template temperature `rv_template_teff` ≥ 8500 K, it is recommended to use the correction derived in Blomme et al. (2023) instead of Eq. (5) above.

Figure 6 (bottom right) presents the median residuals of the radial velocity as a function of `grvs_mag` magnitude after applying the radial velocity correction to the five reference catalogues APOGEE, GALAH, GES, LAMOST, and RAVE. The stars were selected in the same two groups we used to assess the magnitude trends. Group B (giants) is shown in the upper panel, and group A (dwarfs and turn-off stars) are shown in the lower panel. After correction, APOGEE, GALAH, GES, and RAVE samples (both dwarfs and giants) no longer show any statistically significant trend. On the other hand, the LAMOST stars present a trend that reaches approximately 1.5 to 2 km s$^{-1}$ at `grvs_mag` = 14 mag. Since the effect is only visible in the LAMOST DR7 data, it is likely intrinsic to this catalogue. We note that a significant positive bias in LAMOST radial velocities has already been mentioned in previous studies after comparisons to other catalogues (e.g. Huang et al. 2018; Tsantaki et al. 2022).

### 6.2. Atmospheric parameter trends

In this section, we assess how the radial velocity systematic differences between *Gaia* DR3 and the APOGEE, GALAH, GES, RAVE, and LAMOST catalogues depend on the atmospheric parameters, that is, the effective temperature, surface gravity and metallicity. In order to avoid mixing the effects, specific samples are selected for each parameter.

Figure 7 presents the medians of the radial velocity residuals as a function (row 1) of surface gravity for samples of metal-rich giants, (row 2) of effective temperature for samples of metal-rich main-sequence stars, and (rows 3 and 4) of metallicity for samples of giants and main-sequence stars. The selection of the samples is described in Appendix D. The surface gravity and effective temperature plots present the absolute differences between *Gaia* DR3 and the comparison catalogues. Conversely, the median residual curves as a function of metallicity are adjusted vertically by subtracting the median value of the radial velocity residuals measured in the metallicity range [Fe/H] ∈ [−0.25, 0.25] dex. Therefore, the metallicity trends are presented relative to solar metallicity. All samples are corrected for the magnitude trend (Eq. (5)).

APOGEE, GALAH, and to some extent GES present similar trends, and their median radial velocity differences with *Gaia* DR3 are mostly in the range [−500, +500] m s$^{-1}$. The three surveys show a negative correlation with metallicity when compared to *Gaia* DR3, similar to the previous findings of

Tsantaki et al. (2022) for *Gaia* DR2. RAVE does not show the same trends as the three first comparison catalogues, but its median differences with respect to *Gaia* DR3 are also mostly limited to ±500 m s$^{-1}$, except for $T_{\rm eff} > 7000$ K, where the offset between the two catalogues reaches approximately $-1$ km s$^{-1}$. This degradation for hot stars was already noted by Steinmetz et al. (2020b) when they compared RAVE DR6 to *Gaia* DR2. They explained the larger offset and spread by the hydrogen Paschen lines dominating the ionised calcium triplet in the RAVE and RVS spectral range. Steinmetz et al. (2020b) also reported a metallicity dependence of the offset between RAVE DR6 and *Gaia* DR2 radial velocities, which is still present in the comparison with *Gaia* DR3 giant stars. The offsets between LAMOST and *Gaia* DR3 are larger. They vary between +4 and +6 km s$^{-1}$, depending on temperature and gravity. The metallicity trend presents an amplitude of approximately 2 km s$^{-1}$. The comparison between *Gaia* DR2 and LAMOST DR6 by Tsantaki et al. (2022) already showed trends at the same level. In this section, we compare the *Gaia* DR3 radial velocities to the raw LAMOST DR7 radial velocities. We note that Zhang et al. (2021) provided calibrations of LAMOST DR7 radial velocity zeropoints based on *Gaia* DR2 radial velocities.

The *Gaia* DR3 radial velocities presented here are not corrected for the gravitational redshift, which shifts the measurements by a few 10 m s$^{-1}$ in giants and several hundred m s$^{-1}$ in dwarfs (Lindegren & Dravins 2003), nor for the convective shift produced by convective motions in stellar atmospheres. We therefore compared *Gaia* DR3 velocities to estimates that did not take these effects into account either. We note, however, that the GALAH catalogue also provides a measurement of the radial velocity that is corrected for the gravitational redshift and the convective shift (Buder et al. 2021; Zwitter et al. 2021).

In this section, we have considered temperature trends up to $T_{\rm eff} \sim 7500$ K. Blomme et al. (2023) studied the hotter stars and showed that after correcting for the hot star magnitude trend, for $T_{\rm eff} \geq 7500$ K, the absolute value of the *Gaia* DR3 median radial velocity bias is mostly smaller than 3 km s$^{-1}$.

## 7. Validation of the formal uncertainties

The formal uncertainty on the measurement of the combined radial velocity is published in the field `radial_velocity_error`. To evaluate the reliability of the formal uncertainties, we compared our data to the APOGEE DR17 catalogue (Abdurro'uf et al. 2022). In the perfect case, if both *Gaia* DR3 and APOGEE uncertainties were the true and if all stars were constant (i.e. included no binary or variable), the distribution of the radial velocity residuals divided by the combined true uncertainties should follow a normal distribution of standard deviation equal to 1. Conversely, a normalised radial velocity residual can be defined as

$$V_{\rm res}^{\rm norm} = \frac{V_{\rm R} - V_{\rm APO}}{\sqrt{(f_\sigma \times \epsilon_{V_{\rm R}})^2 + \epsilon_{\rm APO}^2}}, \qquad (6)$$

where $V_{\rm R}$ and $\epsilon_{V_{\rm R}}$ are a *Gaia* DR3 combined radial velocity and its associated formal uncertainty, respectively, $V_{\rm APO}$ and $\epsilon_{\rm APO}$ the same quantities for the APOGEE catalogue, and $f_\sigma$ is the multiplicative factor that should be applied to the formal uncertainty $\epsilon_{V_{\rm R}}$ in order to obtain a distribution of $V_{\rm res}^{\rm norm}$ with a standard deviation[2] equal to 1. The coefficient $f_\sigma$ provides a measurement of

---

[2] We used a robust estimator of the standard deviation: $\sigma$ = (Per(84.15) − Per(15.85))/2, where Per(15.85) and Per(84.15) are the 15.85th and 84.15th percentiles of the distribution, respectively.

the reliability of the formal uncertainty. As a caveat, we note that APOGEE uncertainties can also be subject to some imprecision, and that this will reflect on the value derived for $f_\sigma$. Hereafter, we use the same terminology as in Babusiaux et al. (2023), and we refer to $f_\sigma$ as the standard error factor (also referred to as unit weight error in the literature).

To measure the reliability of the formal uncertainties, it is important to use a sample containing as few variable stars as possible. We therefore selected a sub-sample of the APOGEE catalogue with at least four APOGEE measurements (NVISITS ≥ 4) and a scatter of the individual APOGEE radial velocities VSCATTER ≤ 0.5 km s$^{-1}$. We calculated the APOGEE uncertainties as $\epsilon_{\rm APO}$ = VSCATTER/$\sqrt{\rm NVISITS}$. The sub-sample was then further split into several dwarf and giant star samples: from g1 at the top of the giant branch, $\log g \in [-0.5, 1.0]$, to g4 at the bottom, $\log g \in [3.0, 4.0]$, and from d1 at the cool end of the main sequence, $T_{\rm eff} \in [3000, 4000]$ K, to d5 at the hot end, $T_{\rm eff} \in [7000, 8000]$ K. Figure E.1 shows the selection of the giant and dwarf star samples in the Kiel diagram.

Figure 8 shows the standard error factor as a function of `grvs_mag` magnitude for the giant (row 1) and dwarf samples (row 2). Although in detail, the values of $f_\sigma$ vary from sample to sample, several overall trends emerge. On the one hand, the standard error factor decreases with magnitude up to `grvs_mag` = 12 mag and then remains roughly constant in the giant star sample and even increases slightly with magnitude in the dwarf star samples. This transition corresponds to the change in method with which the combined radial velocities as well as their formal uncertainties were calculated (see Sect. 3.6.2). On the other hand, the standard error factor is larger than 1 for `grvs_mag` < 11−12 mag and mostly smaller than 1 beyond, indicating that the formal uncertainties are somewhat under-estimated on the bright side and over-estimated on the faint one. Moreover, for the bright stars, the reliability of the uncertainties improves with increasing gravities (giants) and decreasing temperatures (dwarfs).

As discussed above, the potential under- or over-estimation of the APOGEE uncertainties would modify the estimation of the standard error factor. The $f_\sigma$ values provided in Fig. 8 should not be considered as calibrations, but as illustrations of the overall behaviour of the formal uncertainties. In order to bypass the question of the reliability of the uncertainties of the comparison catalogue, the *Gaia* validation group conducted a similar study (Babusiaux et al. 2023) using the catalogue of wide binaries of El-Badry et al. (2021). One of the merits of this approach is that it relies on *Gaia* DR3 radial velocities and formal uncertainties only. On the other hand, the selected sample is too small to split it into several groups of dwarfs and giants. Babusiaux et al. (2023) proposed a global calibration of $f_\sigma$ as a function of magnitude. It is represented in Fig. 8 by the red curve. It exhibits a trend broadly similar to those of the giant and dwarf star samples.

Figure 8 (row 3) shows two examples of distributions of normalised residuals of groups of stars from the g2 giant sample, selected in the magnitude ranges `grvs_mag` ∈ [9.4, 9.9] (left) and [13.8, 14.1] mag (right), respectively. The normalised residuals are calculated following Eq. (6) using the values of $f_\sigma$ of the g2 sample shown in Fig. 8 (row 1). Gaussian profiles with standard deviations equal to 1 are overlaid (orange curves). The distributions and profiles agree satisfactorily, indicating that at first order, the *Gaia* DR3 radial velocity errors follow a Gaussian distribution.

## 8. Median formal precision

In this section, we assess the median formal precision of the *Gaia* DR3 combined radial velocities as a function of the
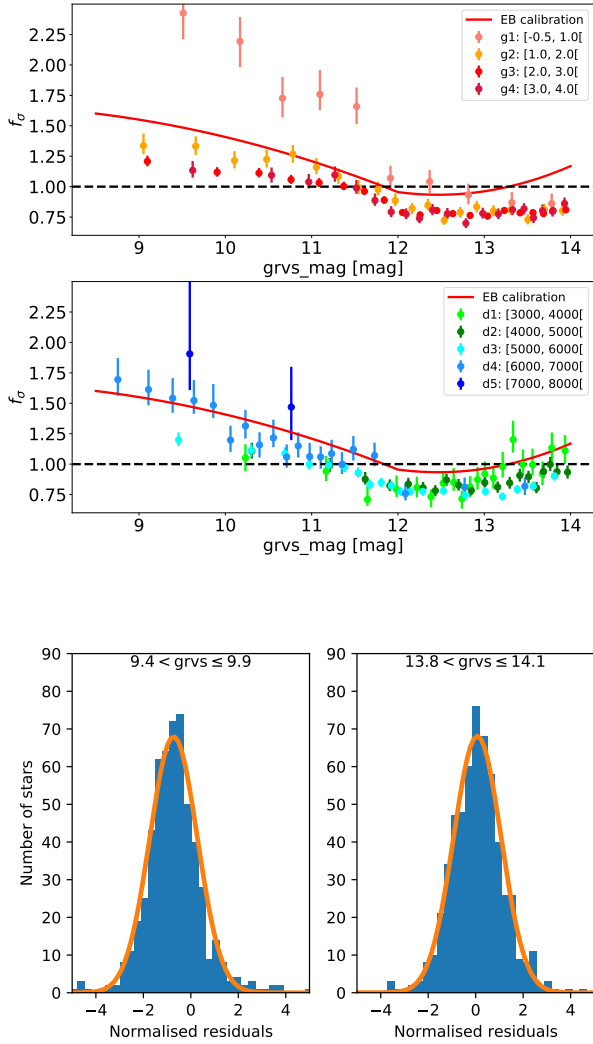
**Fig. 8.** *From top to bottom, row 1*: standard error factor (see text) as a function of grvs_mag magnitude for the giant star samples. The range of surface gravity of each sample is provided in the legend. The red curve corresponds to the calibration of $f_\sigma$ provided in Babusiaux et al. (2023). *Row 2*: same as row 1 for the dwarf star samples. The range of effective temperature of each sample is provided in the legend. *Row 3*: distributions of the normalised residuals of two groups of stars from the g2 giant sample (see Appendix E), selected in the magnitude ranges grvs_mag ∈ [9.4, 9.9] (*left*) and [13.8, 14.1] mag (*right*). Gaussian profiles with standard deviations equal to 1 are overlaid (orange curves).

magnitude and atmospheric parameters on the one hand and, on the other hand, of the galactic coordinates $(l, b)$. For a given sample of stars, the median formal precision is calculated as the median of their radial velocity formal uncertainties: that is, the median of their radial_velocity_error. The lower and upper boundaries of the 68.3% confidence interval on the estimation of the median formal precision are calculated as

$$\epsilon_{\text{prec}}^{\text{low}} = \sqrt{\frac{\pi}{2N}} (\tilde{\epsilon}_{V_R} - \text{Per}(\epsilon_{V_R}, 15.85)) \quad (7)$$

$$\epsilon_{\text{prec}}^{\text{upp}} = \sqrt{\frac{\pi}{2N}} (\text{Per}(\epsilon_{V_R}, 84.15) - \tilde{\epsilon}_{V_R}) \quad (8)$$

where $N$, $\tilde{\epsilon}_{V_R}$, $\text{Per}(\epsilon_{V_R}, 15.85)$ and $\text{Per}(\epsilon_{V_R}, 84.15)$ are the number of elements, the median, and the 15.85th and 84.15th percentiles of the distribution of radial_velocity_error, $\epsilon_{V_R}$, respectively.

The median formal precision of the *Gaia* DR3 radial velocities considered as a whole is $1.3\,\text{km s}^{-1}$ at grvs_mag = 12 mag and $6.4\,\text{km s}^{-1}$ at grvs_mag = 14 mag. Figure 9 presents the median formal precision as a function of magnitude for samples selected along the giant branch (row 1), selected along the main sequence (row 2), and of giants and dwarfs, respectively, selected in different intervals of metallicity (rows 3 and 4). The definition of the groups is based on the template parameters rv_template_teff, rv_template_logg, and rv_template_fe_h. The giant star samples are ordered by increasing surface gravities, from g1 at the top of the giant branch to g4 at the bottom. The dwarf star samples are ordered by increasing temperature from d1 (rv_template_teff ≤ 3750 K) to d7 (rv_template_teff ≥ 10 000 K). In rows 1 and 2, the giant and dwarf samples are restricted to the metallicity range rv_template_fe_h ∈ [−0.5, 0.5] dex. In rows 3 and 4, the giant and dwarf samples combine the g2 and g3 and the d2 and d3 datasets, respectively. Figure F.1 shows the selection of the giant and dwarf star samples in the (rv_template_teff, rv_template_logg) plane.

In *Gaia* DR3, the typical median formal precisions for a solar metallicity red clump star (g3 sample) are $\sim$125 m s$^{-1}$ at grvs_mag = 6 mag, $\sim$230 m s$^{-1}$ at grvs_mag = 10 mag and $\sim$5.2 km s$^{-1}$ at grvs_mag = 14 mag. As shown in Fig. 9 (row 1), the median formal precision weakly depends on the surface gravity. Beyond grvs_mag $\sim$11 mag, the median formal precision from the bottom to the top of the giant branch improves modestly. Conversely, the median formal precision improves significantly as the effective temperature decreases, in particular between 15 000 and 6000 K (Fig. 9, row 2). This reflects the evolution of the information contained in the spectra. In hot stars, it is dominated by broad and shallow lines of the Paschen series. When the temperature decreases, these are gradually replaced by the ionized calcium triplet as well as by numerous sharp neutral lines, which are better suited for measuring radial velocities. Finally, the median formal precision improves with metallicity in giants and dwarfs (Fig. 9, rows 3 and 4). This is the expected behaviour: the lines become stronger with increasing abundances. At magnitude grvs_mag = 12 mag, a very slight shift is visible in some curves, notably those of the dwarfs (rows 2 and 4). This effect is produced by the change in method with which the combined radial velocity and its formal uncertainty were calculated (see Sect. 3.6.2). At magnitude 12 and for dwarf stars, the median formal precision of the robust method is usually 10−15% better than that of the modelling method. For giant stars, the differences in formal precision are much smaller.

As discussed in Sect. 7, the formal uncertainties are somewhat under-estimated for grvs_mag < 11−12 mag, and over-estimated for fainter stars. However, the data used to draw the general trend do not allow an accurate definition of a correction factor as a function of both magnitude and atmospheric parameters. In this section, the median formal precision is therefore derived from uncorrected formal uncertainties. The standard error factor ($f_\sigma$) calculated in Sect. 7 would modify the typical median formal precisions of the solar metallicity red clump star considered above in the following way: at grvs_mag = 6 mag, from $\sim$125 to 150 m s$^{-1}$ (assuming the trend is flat for grvs_mag < 9 mag), at grvs_mag = 10 mag, from $\sim$230 to 260 m s$^{-1}$, and at grvs_mag = 14 mag, from $\sim$5.2 to 4.2 km s$^{-1}$. The impact would be stronger on the bright hot dwarfs ($T_{\text{eff}} > 6000$ K) and on the stars at the tip of the giant branch (sample g1).

**Fig. 10.** Sky map of the median formal precision of all the combined radial velocities of the *Gaia* DR3 catalogue. The image uses a Mollweide projection in Galactic coordinates $(l, b)$. The Galactic centre is at the centre of the image, and the Galactic longitudes increase to the left. The sampling of the map is approximately 0.2 square degree (healpix level 7).

fore driven by the scan law. Conversely, in the densest regions toward the Galactic centre, the median formal precision is about $1 \, \mathrm{km \, s^{-1}}$, although the number of transits there is low. As discussed in Sect. 5.2, only a few faint stars are observed in these regions. This skews the magnitude distribution towards bright stars whose radial velocity measurements are more precise.

# 9. High-velocity stars

In order to observe the largest possible fraction of *Gaia* sources, the RVS has to collect spectra with very low S/N. Even after combining the transits, half of the sources with a radial velocity published in *Gaia* DR3 have an `rv_expected_sig_to_noise` that is lower than 7.8 (see Sect. 5.2). This is quite specific to *Gaia* DR3, as large stellar spectroscopic surveys usually present higher median S/N. As described in Sect. 4.3.2, at very low S/N, the amplitude of the true cross-correlation peak might be lower than that of the highest noise peak(s). The measured radial velocity is then random and obviously incorrect.

Figure 11 (top) presents several radial velocity distributions. The 37 499 608 combined radial velocities produced by the pipeline are shown in salmon. The 33 812 183 sources that successfully passed the validation filters (including a cut at $S/N = 2$) and have published radial velocities in *Gaia* DR3 are shown in black. The cyan and green histograms correspond to the 25.3 and 13.3 million sources with published velocities and `rv_expected_sig_to_noise` $\geq 5$ and 10, respectively. The salmon histogram exhibits flat extended wings. They are populated by the spurious radial velocity measurements. As expected from the random nature of incorrect secondary cross-correlation peaks, these spurious velocities follow a pseudo-uniform distribution, and they dominate in the wings of the radial velocity distribution, which are less strongly populated than the core. The black histogram shows that the validation filters have largely removed the wings and therefore suppressed a very large part of the spurious values. It is rewarding to see the high-velocity GC NGC 3201 emerging after the filters were applied. However, as discussed in Sect. 5.4, the *Gaia* DR3 velocities still exhibit small wings beyond $|V_R| \gtrsim 500-600 \, \mathrm{km \, s^{-1}}$.

The impact of the erroneous values depends on the science case considered. The number of outliers is rather small compared to the full sample. Therefore, it should have little influence on the

**Fig. 9.** *From top to bottom, row 1*: median formal precision as a function of grvs_mag magnitude for different samples of metal-rich stars selected along the giant branch. The range of rv_template_logg of each sample is provided in the legend. *Row 2*: same as row 1 for samples of metal-rich stars selected along the main sequence. The range of rv_template_teff of each sample is provided in the legend. *Row 3*: same as row 1 for giant stars, selected in different ranges of metallicity. The range of rv_template_fe_h of each sample is provided in the legend. *Row 4*: same as row 1 for dwarf stars, selected in different ranges of metallicity. The range of rv_template_fe_h of each sample is provided in the legend. The 68.3% confidence interval on the measurements of the median formal precision is represented as shaded areas.

Figure 10 presents the map of the median formal precision as a function of Galactic longitudes and latitudes. The comparison to Fig. 3 (top) shows that over most of the sky, the median formal precision correlates with the number of transits and is there-

**Fig. 11.** *Top*: distributions of the radial velocities of the 37 499 608 sources successfully processed by the pipeline (salmon), the 33 812 183 *Gaia* DR3 sources (black), the 25.3 million *Gaia* DR3 sources with rv_expected_sig_to_noise $\geq 5$ (cyan), and the 13.3 million *Gaia* DR3 sources with rv_expected_sig_to_noise $\geq 10$ (green). *Middle*: number of *Gaia* DR3 sources with $|V_R| \geq 750\,\mathrm{km\,s^{-1}}$ and an rv_expected_sig_to_noise higher than or equal to the abscissa value. *Bottom*: number of *Gaia* DR3 sources with an rv_expected_sig_to_noise higher than or equal to the abscissa value.

studies of the overall kinematic and dynamical properties of the Milky Way. For all studies that are directly concerned with high-velocity stars, the level of contamination in *Gaia* DR3 poses a problem. The main origin of the spurious measurements are the very low S/N. Unsurprisingly, the cyan and green histograms show that further restricting the data to S/N higher than 5 and 10 gradually removes most of the incorrect high-velocity stars.

This is at the cost of a significant loss of completeness of the sample.

Figure 11 (middle) shows the number of *Gaia* DR3 sources with $|V_R| \geq 750\,\mathrm{km\,s^{-1}}$ and rv_expected_sig_to_noise higher than or equal to the abscissa value. Figure 11 (bottom) shows the total number of *Gaia* DR3 sources with an S/N higher than or equal to the abscissa value. The stars with an absolute value of the radial velocity higher than $750\,\mathrm{km\,s^{-1}}$ are supposed to be extremely rare in the Galaxy. They are used here as a sample representative of a very strong contamination by spurious radial velocities. The *Gaia* DR3 catalogue contains 254 of these stars. This number drops to 13 for an S/N cut-off of 5 and to 1 for a cut-off of 8. At the same time, these cuts reduce the number of sources from initially 33 812 183 to 25 302 443 and 16 476 280, respectively. We recommend that *Gaia* DR3 users who work on high-velocity stars apply a stricter filter on the S/N. Where to set the threshold must be defined according to the science case considered, based on the curves in Fig. 11.

We also recall that low S/N are not the only possible source of spurious high-velocity stars, although they represent by far the main source. Contamination by a bright neighbour can also produce high-velocity outliers (Boubert et al. 2019). Specific filters have been applied to cope with this problem (see Sect. 4.3.3), but problematic sources may have slipped through. We therefore recommend caution with high-velocity stars in the vicinity of a brighter neighbour.

The ground-based surveys described in Appendix C can provide additional insight into the spurious high velocities. To facilitate comparison, the five catalogues were combined into a single dataset. A correction factor of $5\,\mathrm{km\,s^{-1}}$ was subtracted from the LAMOST radial velocities to adjust them to approximately the same scale as the other catalogues. Figure 12 (top left) compares the *Gaia* DR3 radial velocities to those of the combined dataset. Most of the sources are distributed along the main diagonal, which shows the overall good agreement between the *Gaia* DR3 and the ground-based surveys. However, *Gaia* DR3 spurious high velocities are visible as a diffuse vertical sequence centred on $V_R^{GB} \sim 0\,\mathrm{km\,s^{-1}}$. When the comparison is restricted to the sources with rv_expected_sig_to_noise higher than or equal to 5 (Fig. 12, top right), a significant fraction of the spurious sequence and in particular the highest values are removed. Further restricting the dataset to $S/N \geq 10$ removes a few more outliers (Fig. 12, bottom left).

In this section, we discussed the contamination of the high-velocity tails by spurious values. On the other hand, *Gaia* DR3 also contains numerous reliable high velocities. Figure 12 (bottom right) shows a zoomed-view of the velocity ranges $[-600, -300]$ and $[300, 600]\,\mathrm{km\,s^{-1}}$ from the top left panel. The blue shaded area delimits a zone of $\pm 15\,\mathrm{km\,s^{-1}}$ around the main diagonal. Most of the sources are contained within this area, illustrating the consistency of *Gaia* DR3 velocities with those measured from the ground for these high-velocity stars. Here again, the high-velocity GC NGC 3201 appears as an over-density.

## 10. Some specific objects

### 10.1. Open clusters

The combined radial velocities were tested with open clusters, as in *Gaia* DR2. We show two examples here, NGC 2516 and Mamajek 4.

NGC 2516 is a well-studied and populated cluster. A mean radial velocity of $23.82 \pm 0.18\,\mathrm{km\,s^{-1}}$ was previously determined
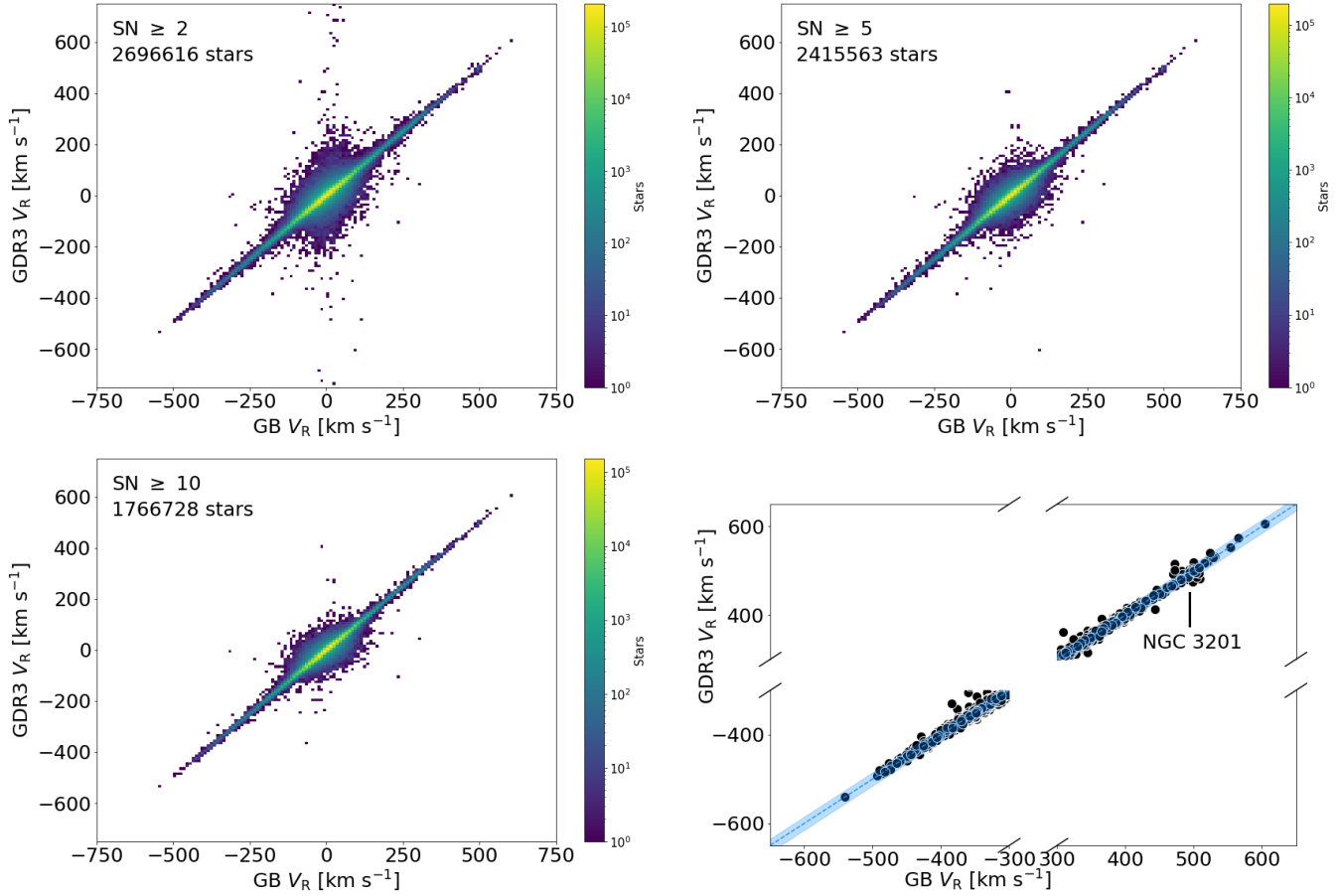
**Fig. 12.** *Top left*: comparison of the *Gaia* DR3 radial velocities to those of the combined dataset (see text). *Top right*: same as the top left panel for stars with rv_expected_sig_to_noise ≥ 5. *Bottom left*: same as the top left panel for stars with rv_expected_sig_to_noise ≥ 10. *Bottom right*: zoomed-view of the velocity ranges $[-600, -300]$ and $[300, 600]$ km s$^{-1}$ from the top left panel. The stars are represented individually. The blue shaded area delimits a zone of $±15$ km s$^{-1}$ around the main diagonal.

by Soubiran et al. (2018a), based on the *Gaia* DR2 RVS data of 132 members identified by Cantat-Gaudin et al. (2018). Tarricq et al. (2021) combined radial velocities from *Gaia* DR2 with those from GALAH DR3 (Buder et al. 2021) and the *Gaia*-ESO survey (Gilmore et al. 2012; Randich et al. 2013) and computed a mean RV of 24.24±0.07 km s$^{-1}$ based on 490 members from Cantat-Gaudin et al. (2018). Tarricq et al. (2022) determined new memberships for this cluster on a large area of sky based on *Gaia* EDR3, which revealed an extended tidal tail and a halo. We find that 826 of these members have a radial velocity in *Gaia* DR3, giving a median radial velocity of 23.51 km s$^{-1}$. The sky distribution of the members is presented in Fig. 13 (top). It confirms the extension of the cluster, with stars in the tidal tail sharing the same motion as the cluster. Figure 13 (bottom) shows the radial velocities of the cluster members as a function of $G$ magnitude after applying the correction of the magnitude trend of the hot stars recommended in Blomme et al. (2023). It shows the consistency of the radial velocities below $G \sim 6.5$ and above $G \sim 10.5$ mag. The range of apparent magnitude $G \in [6.5, 10.5]$ mag corresponds to the upper main sequence of NGC 2516 and is populated by hot stars with rv_template_teff ≥ 8500 K. They exhibit residual offsets of a few km s$^{-1}$, as described in Blomme et al. (2023).

In contrast, Mamajek 4 is a loose and poorly studied cluster. Its mean radial velocity, $-26.32±0.54$ km s$^{-1}$, in Soubiran et al. (2018a) was based on 34 members. Tarricq et al. (2021)

reported that 41 members with radial velocities from *Gaia* DR2 and GALAH gave a mean value of $-27.25±0.34$ km s$^{-1}$. Tarricq et al. (2022) found a tidal tail and a halo for this cluster as well. On the basis of these new memberships covering a large area, we find 196 members with a combined radial velocity in *Gaia* DR3 giving a median value of $-29.45$ km s$^{-1}$. Figure 14 presents the spatial distribution (top) and the radial velocities (also corrected for the hot star magnitude trend) as a function of $G$ magnitude (bottom) of Mamajek 4.

### 10.2. Globular clusters

In this section, we consider as GC members the stars from the catalogue of Vasiliev & Baumgardt (2021) with a membership probability higher than 90%. The increase in limiting magnitude of the spectroscopic processing has also benefited the GC. Out of the list of 170 GC published in Vasiliev & Baumgardt (2021), radial velocities are published for 111 in *Gaia* DR3. The number of members with a *Gaia* DR3 radial velocity varies greatly from one cluster to the next, from more than 1000 in NGC 5139 (Omega Cen) and NGC 104 (47 Tuc) to 5 in Terzan 5 and NGC 6522 (which is located in Baade's Window). Figure 15 shows the distribution of the 111 GC on the celestial sphere in Galactic coordinates $(l, b)$, as well as the number of radial velocity measurements in each of them.
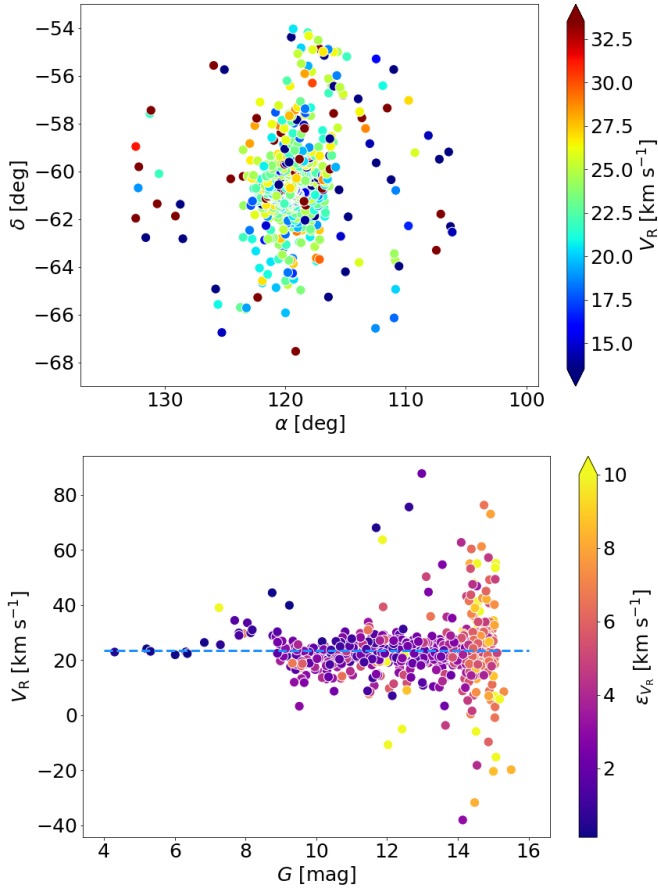
**Fig. 13.** *Top*: spatial distribution of the stars of the open cluster NGC 2516. *Bottom*: *Gaia* DR3 combined radial velocities as a function of $G$ magnitude for the stars of the open cluster NGC 2516. The correction of the magnitude trend of the hot stars recommended in Blomme et al. (2023) is applied.

**Fig. 14.** Same as Fig. 13 for the open cluster Mamajek 4.

To further illustrate the properties of the radial velocities measured in GC, we considered the case of 47 Tuc. Figure 16 (top left) shows its colour-magnitude diagram, $G$ versus $G_{BP}-G_{RP}$. The stars with *Gaia* EDR3 photometry are represented as grey dots, and those with a *Gaia* DR3 radial velocity are colour-coded according to the formal uncertainty in radial velocity. The limit of the spectroscopic processing is visible as a relatively sharp cut around $G \sim 15$ mag. The radial velocity measurements cover the upper part of the red giant branch, the asymptotic giant branch, and the horizontal branch. The formal uncertainties improve with magnitude and are about a few km s$^{-1}$ at the level of the horizontal branch and a few hundred m s$^{-1}$ at the tip of the red giant branch.

The radial velocities are measured throughout the cluster, including the densest regions of the core. However, two of the issues encountered in the most crowded regions of the bulge (see Sect. 5.2) also apply to the central parts of the cluster: (i) the limit to 72 of the number of windows that can be allocated simultaneously per CCD and, (ii) the numerous conflicts between windows, part of which cannot be resolved (e.g. because the sources are too close to each other). The consequences are similar to those witnessed before. The number of transits per source is very low in the central part of the cluster and increases outward (Fig. 16, top right). Moreover, the limiting magnitude of the sources with measured velocities drops in the core of the cluster (Fig. 16, middle left). Because of this selection effect, the formal



**Fig. 15.** Distribution on the sky of the 111 GC containing stars whose radial velocities are published in *Gaia* DR3. The colour code indicates the number of stars with measured velocity in each cluster. The image uses an Aitoff projection in Galactic coordinates ($l, b$). The Galactic centre is at the centre of the image, and the Galactic longitudes increase to the left. Clusters with more than 200 members with a *Gaia* DR3 radial velocity are circled in black, and their names are reported on the plot.

uncertainties on the radial velocity measurements are globally smaller in the centre of the cluster (Fig. 16, middle right).

The high stellar density makes the observation conditions in the GC peculiar. It may therefore be wondered whether the formal uncertainties remain reliable in these objects. To answer this question, we used a sample of stars whose velocities were measured from the ground and are compiled in Baumgardt & Hilker (2018). Using this sample, we assessed the radial velocity

precision in two different ways. The median formal precision was calculated as the median of the formal uncertainties in radial velocity (as in Sect. 8). The external precision was computed as the robust standard deviation of the radial velocity residuals (*Gaia* minus ground-based). Figure 16 (bottom left) compares the two precision curves. Overall, they agree satisfactorily, although with a $\sim 1.5\sigma$ discrepancy at $G \sim 14.5$. Therefore, the radial velocity formal uncertainties also appear to be reliable in dense regions, such as GC.

The large number of measured radial velocities allows studying the internal motions of the stars within the cluster. In Fig. 16 (bottom right), the stars are colour-coded according to their *Gaia* DR3 combined radial velocity. Their precisions make it possible to clearly visualise the line-of-sight rotational velocity of 47 Tuc. It is traced by the gradient of the radial velocities, which vary from blue at the top left to yellow-red at the bottom right. Combined with the proper motions, the *Gaia* DR3 radial velocities should provide a detailed insight into the kinematic of 47 Tuc and of similarly sampled objects.

### 10.3. Large magellanic cloud

The extension of the radial velocity catalogue down to magnitude $G_{\rm RVS}^{\rm ext} = 14$ has increased the number of stars observed in nearby galaxies. The best sampled of these objects is the Large Magellanic Cloud. In this section, we study the properties of the radial velocities measured in the LMC.

The selection of the LMC stars is performed in several steps. First, stars within a radius of $10°$ from the centre of the LMC $((\alpha, \delta) = (81.28°, -69.78°),$ van der Marel 2001) were extracted from the *Gaia* DR3 database. Then the foreground stars were removed, keeping the stars with $\varpi/\epsilon_\varpi < 5$. Finally, the sample was restricted to stars with a combined radial velocity higher than $150\,{\rm km\,s^{-1}}$, in order to mitigate the contamination by stars with disc velocities. The selected sample contains 29 631 stars. It is made of asymptotic giant branch (AGB) and blue loop (BL) stars (using the selection and terminology of Gaia Collaboration 2021b; see their Fig. 2). The sample contains only 56 stars with $\mathtt{rv\_template\_teff} \geq 7000\,{\rm K}$, including 12 stars hotter than 8500 K. The reason for this low proportion is twofold. On the one hand, these stars are blue and therefore fainter in the RVS infrared band. Moreover, in GDR3, the limiting magnitude for hot stars is $G_{\rm RVS}^{\rm ext} = 12\,{\rm mag}$, but 14 for the cooler stars. We recall that Blomme et al. (2023) recommend to apply a specific magnitude-dependent correction (their Eq. (1)) to stars with $8500 \leq \mathtt{rv\_template\_teff} \leq 14\,500\,{\rm K}$ and $6 \leq \mathtt{grvs\_mag} \leq 12\,{\rm mag}$. After correction, the systematic radial velocity offset between the stars cooler and hotter than 7000 K should not exceed $\pm 3\,{\rm km\,s^{-1}}$.

Figure 17 shows the distribution in equatorial coordinates of the LMC stars, colour-coded according to their combined radial velocities. They exhibit a clear gradient, from $\sim 320\,{\rm km\,s^{-1}}$ (red) at the top to $\sim 200\,{\rm km\,s^{-1}}$ (blue) at the bottom, which maps the rotation of the LMC projected onto the line of sight. The combined radial velocities will complement the *Gaia* EDR3 astrometric and photometric measurements (Gaia Collaboration 2021a; Lindegren et al. 2021; Riello et al. 2021), which already provided a detailed view of the structure and properties of the LMC (Gaia Collaboration 2021b).

## 11. Radial velocity variability

*Gaia* DR3 contains two radial velocity variability indices. In Sect. 3.7 we proposed to combine them into a single

criterion. Stars with $\mathtt{rv\_chisq\_pvalue} \leq 0.01$ and $\mathtt{rv\_renormalised\_gof} > 4$ are considered variable. This criterion is applicable to stars with $\mathtt{rv\_nb\_transits} \geq 10$ and $\mathtt{rv\_template\_teff} \in [3900, 8000]$.

To assess the performance of this criterion, five datasets were used, two made of constant stars, and the three others of variable stars. The first constant-star sample (hereafter referred to as CS18) was extracted from the catalogue of Soubiran et al. (2018b), selecting the stars with at least two measurements in this catalogue, with 300 days at least between the first and the last measurement and with a standard deviation of the radial velocity measurements smaller than or equal to $100\,{\rm m\,s^{-1}}$. The second sample of constant stars comes from the APOGEE DR17 catalogue (Abdurro'uf et al. 2022). Here also, a subsample of stars was selected based on the number of APOGEE measurements and on their scatter: $\mathtt{NVISITS} \geq 4$ and $\mathtt{VSCATTER} \leq 0.5\,{\rm km\,s^{-1}}$. The first two samples of variable stars are made of 744 and 492 previously known Cepheids and RR-Lyrae, respectively, provided by the *Gaia*-DPAC variability group (G. Clementini, priv. comm.). The last sample of variable stars is made of spectroscopic binaries compiled by T. Morel (priv. comm.) from the series of papers by R. F. Griffin (see Griffin 2019, and previous papers in the series).

Figure 18 presents the result of the classification in the form of a confusion matrix. For each sample (one per column), the percentages of stars classified as constant and as variable, following our proposed criterion, are provided in the top and bottom rows, respectively. The percentages of CS18 and APOGEE stars that are correctly classified as constant are 99.7% and 94.7%, respectively. The success rates are similar for the variables, 97.3% of the Cepheids, 97.2% of the RR-Lyrae and 95.3% of the spectroscopic binaries are classified as variable by the criterion above.

## 12. Conclusions

*Gaia* DR3 contains the combined radial velocities of 33 812 183 stars down to $G_{\rm RVS}^{\rm ext} = 14\,{\rm mag}$. With respect to the first radial velocity catalogue published in *Gaia* DR2, the temperature interval has been expanded from $\mathtt{rv\_template\_teff} \in [3600, 6750]\,{\rm K}$ to $\mathtt{rv\_template\_teff} \in [3100, 14\,500]\,{\rm K}$ for the bright stars ($\mathtt{grvs\_mag} \leq 12\,{\rm mag}$) and $[3100, 6750]\,{\rm K}$ for the fainter stars. The radial velocities sample a significant part of the Milky Way disc, extending a few kilo-parsecs beyond the Galactic centre as well as into the inner halo, up to about $10-15\,{\rm kpc}$. The median formal precision of the velocities is $1.3\,{\rm km\,s^{-1}}$ at $\mathtt{grvs\_mag} = 12$ and $6.4\,{\rm km\,s^{-1}}$ at $\mathtt{grvs\_mag} = 14\,{\rm mag}$. The velocities exhibit a small systematic trend with magnitude starting around $\mathtt{grvs\_mag} = 11\,{\rm mag}$ and reaching about $400\,{\rm m\,s^{-1}}$ at $\mathtt{grvs\_mag} = 14\,{\rm mag}$. A correction formula is provided for this. The *Gaia* DR3 velocity scale agrees satisfactorily with APOGEE, GALAH, GES, and RAVE. The systematic differences mostly do not exceed a few hundred $\mathrm{m\,s^{-1}}$ and are similar to previous findings involving *Gaia* DR2 (see e.g. Steinmetz et al. 2020b; Tsantaki et al. 2022).

*Gaia* DR3 will provide the largest catalogue of stellar radial velocities to date. However, records are made to be broken. *Gaia* DR4 is expected to process all RVS spectra down to the limiting magnitude $G_{\rm RVS}^{\rm on-board} = 16.2\,{\rm mag}$ and is expected to contain the radial velocities of more than 100 million stars. To achieve this objective, the pipeline will have to process a huge volume of spectra with extremely low S/N. The separation of the invalid and valid measurements is the challenge of the next radial velocity catalogue. Specific machine-learning and deep-learning
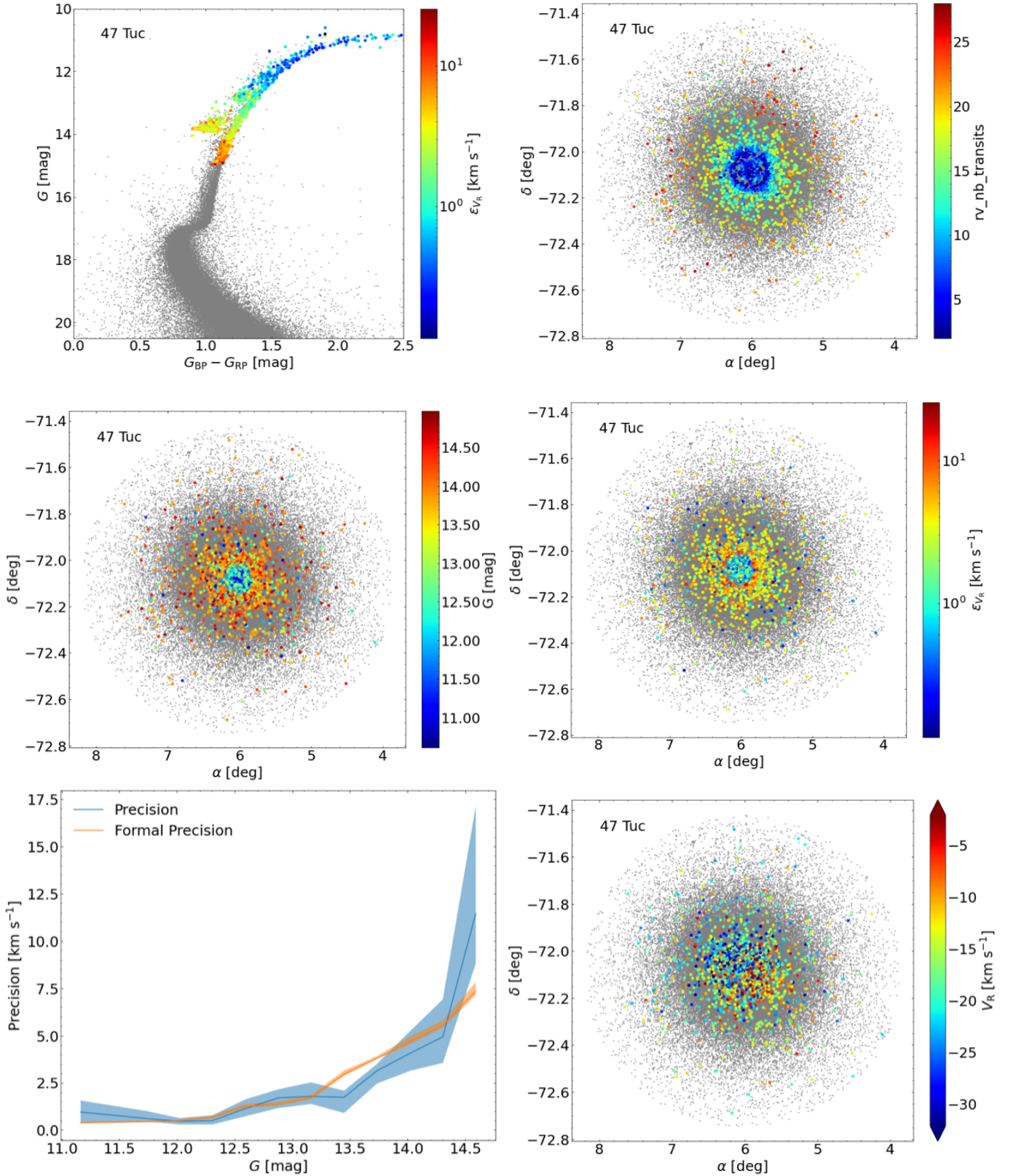
**Fig. 16.** *Top left*: colour-magnitude diagram of 47 Tuc. The stars with *Gaia* EDR3 photometry are represented as grey dots. The stars with a *Gaia* DR3 radial velocity are colour-coded by the formal uncertainties in radial velocity. *Top right*: distribution in equatorial coordinates ($\alpha$, $\delta$) of the 47 Tuc stars. Stars with a *Gaia* DR3 radial velocity are colour-coded by number of transits. *Middle left*: same as in the top right panel, with the stars colour-coded by $G$ magnitude. *Middle right*: same as in the top right panel, with the stars colour-coded by the formal uncertainty in radial velocity. *Bottom left*: comparison of the formal and external precisions (see text) as a function of $G$ magnitude for a sub-sample of 47 Tuc stars. The 68.3% confidence interval on the estimates of the precisions are represented as shaded areas. *Bottom right*: same as in the top right panel, with the stars colour-coded by combined radial velocity.
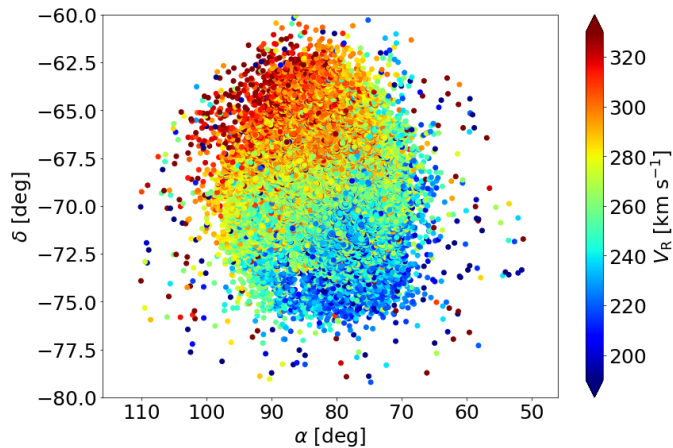
**Fig. 17.** Distribution in equatorial coordinates ($\alpha$, $\delta$) of the LMC stars, colour-coded by combined radial velocities.
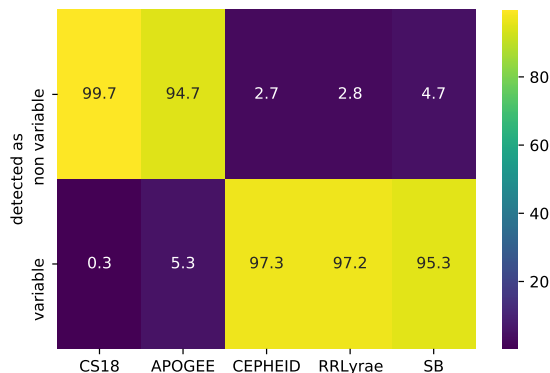


**Fig. 18.** Percentage of stars classified as constant (*top row*) and variable (*bottom row*) for the two samples of constant stars, CS18 and APOGEE, and for the three samples of variable stars, Cepheids, RR-Lyrae, and spectroscopic binaries.

methods are being developed and tested to best identify the spurious velocities, minimise the contamination, and maximise the completeness.

# References

Abdurro'uf, Accetta, K., Aerts, C., et al. 2022, ApJS, 259, 35
Abolfathi, B., Aguado, D. S., Aguilar, G., et al. 2018, ApJS, 235, 42
Andrae, R., Fouesneau, M., Sordo, R., et al. 2023, A&A, 674, A27 (*Gaia* DR3 SI)
Astropy Collaboration (Robitaille, T. P., et al.) 2013, A&A, 558, A33
Astropy Collaboration (Price-Whelan, A. M., et al.) 2018, AJ, 156, 123
Babusiaux, C., Fabricius, C., Khanna, S., et al. 2023, A&A, 674, A32 (*Gaia* DR3 SI)
Bailer-Jones, C. A. L., Rybizki, J., Fouesneau, M., Demleitner, M., & Andrae, R. 2021, AJ, 161, 147
Baumgardt, H., & Hilker, M. 2018, MNRAS, 478, 1520
Baumgardt, H., Hilker, M., Sollima, A., & Bellini, A. 2019, MNRAS, 482, 5138
Bennett, M., & Bovy, J. 2019, MNRAS, 482, 1417
Blomme, R., Frémat, Y., Sartoretti, P., et al. 2023, A&A, 674, A7 (*Gaia* DR3 SI)
Boubert, D., Strader, J., Aguado, D., et al. 2019, MNRAS, 486, 2618
Buder, S., Sharma, S., Kos, J., et al. 2021, MNRAS, 506, 150
Cantat-Gaudin, T., Jordi, C., Vallenari, A., et al. 2018, A&A, 618, A93
Clementini, G., Ripepi, V., Garofalo, A., et al. 2023, A&A, 674, A18 (*Gaia* DR3 SI)
Creevey, O. L., Sordo, R., Pailler, F., et al. 2023, A&A, 674, A26 (*Gaia* DR3 SI)
Cropper, M., Katz, D., Sartoretti, P., et al. 2018, A&A, 616, A5
David, M., Blomme, R., Frémat, Y., et al. 2014, A&A, 562, A97
Delchambre, L., Bailer-Jones, C. A. L., Bellas-Velidis, I., et al. 2023, A&A, 674, A31 (*Gaia* DR3 SI)
Deng, L. C., Newberg, H. J., Liu, C., et al. 2012, RAA, 12, 735
El-Badry, K., Rix, H. W., & Heintz, T. M. 2021, MNRAS, 506, 2269
ESA 1997, in The HIPPARCOS and TYCHO Catalogues. Astrometric and Photometric Star Catalogues Derived from the ESA HIPPARCOS Space Astrometry Mission, ESA Spec. Publ., 1200
Evans, D. W., Riello, M., De Angeli, F., et al. 2018, A&A, 616, A4
Famaey, B., Jorissen, A., Luri, X., et al. 2005, A&A, 430, 165
Frémat, Y., Royer, F., Marchal, O., et al. 2023, A&A, 674, A8 (*Gaia* DR3 SI)
Gaia Collaboration (Prusti, T., et al.) 2016, A&A, 595, A1
Gaia Collaboration (Brown, A. G. A., et al.) 2018, A&A, 616, A1
Gaia Collaboration (Brown, A. G. A., et al.) 2021a, A&A, 649, A1
Gaia Collaboration (Luri, X., et al.) 2021b, A&A, 649, A7
Gaia Collaboration (Bailer-Jones, C. A. L., et al.) 2023a, A&A, 674, A41 (*Gaia* DR3 SI)
Gaia Collaboration (Drimmel, R., et al.) 2023b, A&A, 674, A37 (*Gaia* DR3 SI)
Gaia Collaboration (Vallenari, A., et al.) 2023c, A&A, 674, A1 (*Gaia* DR3 SI)
Gilmore, G., Randich, S., Asplund, M., et al. 2012, The Messenger, 147, 25
Górski, K. M., Hivon, E., Banday, A. J., et al. 2005, ApJ, 622, 759
GRAVITY Collaboration (Abuter, R., et al.) 2022, A&A, 657, L12
Griffin, R. F. 2019, The Observatory, 139, 111
Hambly, N. C., Cropper, M., Boudreault, S., et al. 2018, A&A, 616, A15
Harris, C. R., Millman, K. J., van der Walt, S. J., et al. 2020, Nature, 585, 357
Hoeg, E., Bässgen, G., Bastian, U., et al. 1997, A&A, 323, L57
Høg, E., Fabricius, C., Makarov, V. V., et al. 2000, A&A, 355, L27
Huang, Y., Liu, X. W., Chen, B. Q., et al. 2018, AJ, 156, 90
Hunter, J. D. 2007, Comput. Sci. Eng., 9, 90
Katz, D., Munari, U., Cropper, M., et al. 2004, MNRAS, 354, 1223
Katz, D., Sartoretti, P., Cropper, M., et al. 2019, A&A, 622, A205
Lasker, B. M., Lattanzi, M. G., McLean, B. J., et al. 2008, AJ, 136, 735
Lindegren, L. 2009, Minimum-dimension LSF Modelling, GAIA-C3-TN-LU-LL-084, http://www.rssd.esa.int/doc_fetch.php?id=2915742
Lindegren, L., & Dravins, D. 2003, A&A, 401, 1185
Lindegren, L., Klioner, S. A., Hernández, J., et al. 2021, A&A, 649, A2
Luo, A. L., Zhao, Y. H., Zhao, G., et al. 2015, RAA, 15, 1095
McConnachie, A. W. 2012, AJ, 144, 4
McKinney, W. 2010, in Proceedings of the 9th Python in Science Conference, eds. S. van der Walt, & J. Millman, 51
Nordström, B., Mayor, M., Andersen, J., et al. 2004, A&A, 418, 989
Perryman, M. A. C., Lindegren, L., Kovalevsky, J., et al. 1997, A&A, 323, L49
Perryman, M. A. C., de Boer, K. S., Gilmore, G., et al. 2001, A&A, 369, 339
Randich, S., Gilmore, G., & Gaia-ESO Consortium 2013, The Messenger, 154, 47
Recio-Blanco, A., de Laverny, P., Palicio, P. A., et al. 2023, A&A, 674, A29 (*Gaia* DR3 SI)
Riello, M., De Angeli, F., Evans, D. W., et al. 2018, A&A, 616, A3
Riello, M., De Angeli, F., Evans, D. W., et al. 2021, A&A, 649, A3
Rimoldini, L., Holl, B., Gavras, P., et al. 2023, A&A, 674, A14 (*Gaia* DR3 SI)
Rybizki, J., Rix, H. W., Demleitner, M., Bailer-Jones, C. A. L., & Cooper, W. J. 2021, MNRAS, 500, 397
Sartoretti, P., Katz, D., Cropper, M., et al. 2018, A&A, 616, A6
Sartoretti, P., Blomme, R., David, M., & Seabroke, G. 2022, Gaia DR3 Documentation Chapter 6: Spectroscopy, https://gea.esac.esa.int/archive/documentation/GDR3/Data_processing/chap_cu6spe/
Sartoretti, P., Marchal, O., Babusiaux, C., et al. 2023, A&A, 674, A6 (*Gaia* DR3 SI)
Seabroke, G. M., Fabricius, C., Teyssier, D., et al. 2021, A&A, 653, A160
Smart, R. L., & Nicastro, L. 2014, A&A, 570, A87

Soubiran, C., Cantat-Gaudin, T., Romero-Gómez, M., et al. 2018a, A&A, 619, A155

Soubiran, C., Jasniewicz, G., Chemin, L., et al. 2018b, A&A, 616, A7

Steinmetz, M. 2003, in Gaia Spectroscopy: Science and Technology, ed. U. Munari, ASP Conf. Ser., 298, 381

Steinmetz, M., Zwitter, T., Siebert, A., et al. 2006, AJ, 132, 1645

Steinmetz, M., Guiglion, G., McMillan, P. J., et al. 2020a, AJ, 160, 83

Steinmetz, M., Matijevič, G., Enke, H., et al. 2020b, AJ, 160, 82

Strauss, M. A., Weinberg, D. H., Lupton, R. H., et al. 2002, AJ, 124, 1810

Tarricq, Y., Soubiran, C., Casamiquela, L., et al. 2021, A&A, 647, A19

Tarricq, Y., Soubiran, C., Casamiquela, L., et al. 2022, A&A, 659, A59

Traven, G., Feltzing, S., Merle, T., et al. 2020, A&A, 638, A145

Tsantaki, M., Pancino, E., Marrese, P., et al. 2022, A&A, 659, A95

van der Marel, R. P. 2001, AJ, 122, 1827

van Leeuwen, F. 2007, A&A, 474, 653

Vasiliev, E., & Baumgardt, H. 2021, MNRAS, 505, 5978

Zhang, B., Li, J., Yang, F., et al. 2021, ApJS, 256, 14

Zhao, G., Zhao, Y. H., Chu, Y. Q., Jing, Y. P., & Deng, L. C. 2012, RAA, 12, 723

Zonca, A., Singer, L., Lenz, D., et al. 2019, J. Open Sour. Softw., 4, 1298

Zucker, S. 2003, MNRAS, 342, 1291

Zwitter, T., Kos, J., Buder, S., et al. 2021, MNRAS, 508, 4202

[1] GEPI, Observatoire de Paris, Université PSL, CNRS, 5 Place Jules Janssen, 92190 Meudon, France

[2] CNES Centre Spatial de Toulouse, 18 Avenue Edouard Belin, 31401 Toulouse Cedex 9, France

[3] Mullard Space Science Laboratory, University College London, Holmbury St Mary, Dorking, Surrey RH5 6NT, UK

[4] Université Côte d'Azur, Observatoire de la Côte d'Azur, CNRS, Lagrange UMR 7293, CS 34229, 06304 Nice Cedex 4, France

[5] Royal Observatory of Belgium, Ringlaan 3, 1180 Brussels, Belgium

[6] Observatoire Astronomique de Strasbourg, Université de Strasbourg, CNRS, UMR 7550, 11 Rue de l'Université, 67000 Strasbourg, France

[7] Unidad de Astronomía, Fac. Cs. Básicas, Universidad de Antofagasta, Avda. U. de Antofagasta, 02800 Antofagasta, Chile

[8] CRAAG – Centre de Recherche en Astronomie, Astrophysique et Géophysique, Route de l'Observatoire Bp 63, Bouzareah 16340, Alger, Algeria

[9] Institut d'Astrophysique et de Géophysique, Université de Liège, 19c, Allée du 6 Août, 4000 Liège, Belgium

[10] Universiteit Antwerpen, Onderzoeksgroep Toegepaste Wiskunde, Middelheimlaan 1, 2020 Antwerpen, Belgium

[11] F.R.S.-FNRS, Rue d'Egmont 5, 1000 Brussels, Belgium

[12] Leibniz Institute for Astrophysics Potsdam (AIP), An der Sternwarte 16, 14482 Potsdam, Germany

[13] Laboratoire Univers et Particules de Montpellier, Université Montpellier, CNRS, Place Eugène Bataillon, CC72, 34095 Montpellier Cedex 05, France

[14] Astronomical Institute, Faculty of Mathematics and Physics, Charles University, V Holešovičkách 2, 180 00 Praha 8, Czech Republic

[15] Laboratoire d'Astrophysique de Bordeaux, Université de Bordeaux, CNRS, B18N, Allée Geoffroy Saint-Hilaire, 33615 Pessac, France

[16] Faculty of Mathematics and Physics, University of Ljubljana, Jadranska ulica 19, 1000 Ljubljana, Slovenia

[17] Institut de Ciències del Cosmos, Universitat de Barcelona (IEEC-UB), Martí i Franquès 1, 08028 Barcelona, Spain

[18] Univ. Grenoble Alpes, CNRS, IPAG, 38000 Grenoble, France

[19] ATOS for CNES Centre Spatial de Toulouse, 18 Avenue Edouard Belin, 31401 Toulouse Cedex 9, France

[20] Max Planck Institute for Extraterrestrial Physics, High Energy Group, Gießenbachstraße, 85741 Garching, Germany

[21] Thales Services for CNES Centre Spatial de Toulouse, 18 Avenue Edouard Belin, 31401 Toulouse Cedex 9, France

[22] Department of Astronomy and Theoretical Physics, Lund Observatory, Box 43, 221 00 Lund, Sweden

[23] Telespazio UK S.L. for European Space Agency (ESA), Camino bajo del Castillo s/n, Urbanizacion Villafranca del Castillo, Villanueva de la Cañada 28692, Madrid, Spain

[24] Sorbonne Université CNRS, UMR 7095, Institut d'Astrophysique de Paris, 75014 Paris, France

## Appendix A: *Gaia* DPAC acknowledgements

## Appendix B: *Gaia* DR3 spectroscopy related fields

Table B.1 lists the parameters related to the radial velocity published in *Gaia* DR3. They are all stored in the `gaia_source` table. The computation of `rv_chisq_pvalue`, `rv_renormalised_gof` and, `rv_amplitude_robust` requires reliable epoch radial velocities and is therefore restricted to `grvs_mag ≤ 12` mag. `rv_chisq_pvalue` is further restricted to stars with `rv_nb_transits ≥ 3` and `rv_renormalised_gof` to stars with `grvs_mag ≥ 5.5` mag and `rv_template_teff < 14500` K. In *Gaia* DR3, the radial velocity time series are published for a limited sample of slightly fewer than 2000 Cepheids and RR-Lyrae. They can be identified using the field `has_epoch_rv`, which is set to `True`. Their time series are stored in the table `vari_epoch_radial_velocity`.

Table B.2 lists the parameters produced by the spectroscopic pipeline, which are presented in companion papers. They are all stored in the `gaia_source` table, except `rvs_mean_spectrum`, which is a DataLink product.

**Table B.1.** Radial velocity related fields published in *Gaia* DR3.

| Field | Units | DB column name | Sect. |
|---|---|---|---|
| Combined radial velocity | km s$^{-1}$ | `radial_velocity` | 3.6.2 |
| Combined radial velocity formal uncertainty | km s$^{-1}$ | `radial_velocity_error` | 3.6.2 |
| Combined radial velocity method | | `rv_method_used` | 3.6.2 |
| Number of transits | transits | `rv_nb_transits` | |
| Number of deblended transits | transits | `rv_nb_deblended_transits` | |
| Number of visibility periods | | `rv_visibility_periods_used` | |
| Duration of the radial velocity time series | days | `rv_time_duration` | |
| Expected signal-to-noise ratio | | `rv_expected_sig_to_noise` | |
| Renormalised goodness of fit | | `rv_renormalised_gof` | 3.7 |
| Chi-square P-value | | `rv_chisq_pvalue` | 3.7 |
| Amplitude of the radial velocity time series | km s$^{-1}$ | `rv_amplitude_robust` | 3.7 |
| Template effective temperature | K | `rv_template_teff` | 3.6.1 |
| Template surface gravity | dex | `rv_template_logg` | 3.6.1 |
| Template metallicity | dex | `rv_template_fe_h` | 3.6.1 |
| Origin of the atmospheric parameters | | `rv_atm_param_origin` | 3.6.1 |
| Availability of radial velocity time series | | `has_epoch_rv` | 3.6.1 |

**Table B.2.** Quantities produced by the spectroscopic pipeline and presented in companion papers.

| Field | Units | DB column name | Reference |
|---|---|---|---|
| Median broadening velocity | km s$^{-1}$ | `vbroad` | Frémat et al. (2023) |
| Broadening velocity uncertainty | km s$^{-1}$ | `vbroad_error` | Frémat et al. (2023) |
| Number of vbroad transits | transits | `vbroad_nb_transits` | Frémat et al. (2023) |
| Median $G_{RVS}$ | mag | `grvs_mag` | Sartoretti et al. (2023) |
| $G_{RVS}$ uncertainty | mag | `grvs_mag_error` | Sartoretti et al. (2023) |
| Number of $G_{RVS}$ transits | transits | `grvs_mag_nb_transits` | Sartoretti et al. (2023) |
| Availability of the mean spectrum | | `has_rvs` | Seabroke et al. (in prep.) |
| Signal-to-noise ratio per pixel of the mean spectrum | | `rv_spec_sig_to_noise` | Seabroke et al. (in prep.) |
| Mean spectrum | | `rvs_mean_spectrum` | Seabroke et al. (in prep.) |

# Appendix C: Comparison catalogues

In Sect. 6 (accuracy), Sect. 7 (formal uncertainties), and Sect. 9 (high-velocity stars), the *Gaia* DR3 combined radial velocities are compared to the velocities of one or several of the following catalogues: APOGEE DR17 (Abdurro'uf et al. 2022), GALAH DR3 (Buder et al. 2021; Zwitter et al. 2021), GAIA-ESO Survey (GES) DR3 (Gilmore et al. 2012; Randich et al. 2013), LAMOST DR7 (Zhao et al. 2012; Deng et al. 2012; Luo et al. 2015), and RAVE DR6 (Steinmetz et al. 2020b,a). The selection of the comparison samples is described below.

APOGEE DR17. We used the data from the `allStar-dr17-synspec_rev1.fits` file, including the cross-match with the *Gaia* EDR3 catalogue (which is based on the same list of `source_id` as *Gaia* DR3). For each APOGEE star that was observed multiple times, we kept the occurrence with the highest S/N (`EXTRATARG` fourth binary digit set to 0), and the others were discarded. Stars without a radial velocity measurement in *Gaia* DR3 were removed. Finally, only the stars meeting the following quality criteria were considered: (i) `STARFLAG` 0th (`BAD_PIXELS`) and 3rd (`VERY_BRIGHT_NEIGHBOR`) binary digits set to 0, (ii) `ASPCAPFLAG` 10th (`ROTATION_WARN`), and 23rd (`STAR_BAD`) binary digits set to 0, (iii) valid `VHELIO_AVG`, `TEFF`, `LOGG`, and `FE_H`, and (iv) `N_COMPONENTS` equal to 1. The APOGEE DR17 comparison sample contains 459 998 stars.

GALAH DR3. We used the data from the `GALAH_DR3_main_allstar_v2.fits` file and from the `GALAH_DR3_VAC_rv_v2.fits` file, including the cross-match with the *Gaia* EDR3 catalogue. The duplicated *Gaia* EDR3 `source_id` and stars without a radial velocity measurement in *Gaia* DR3 were removed. Moreover, only the stars meeting the following quality criteria were considered: (i) `snr_c3_iraf` ≥ 30, (ii) `use_rv_flag`, `flag_sp`, and `flag_fe_h` all three equal to 0 and (iii) valid `rv_nogr_obst`, `teff`, `logg`, and `fe_h`. Finally, the 12 760 stars identified as double-line spectroscopic binaries by Traven et al. (2020) were also discarded. GALAH DR3 provides several measurements of the radial velocity. We used the field `rv_nogr_obst`, which is not corrected for the gravitational redshift or for the convective shift. The GALAH DR3 comparison sample contains 294 976 stars.

GES DR3. The data were downloaded from the ESO archive[3]. The cross-match was provided by the *Gaia* catalogue validation group (Babusiaux et al. 2023). Duplicated stars and stars without a radial velocity measurement in *Gaia* DR3 were removed. The following stars were also removed: (i) `TECH` flag set to 9020, 9030, 9050, 15100, 15110, or 15130, (ii) `PECULI` flag set to 2005, 2010, 2020, 2030, 2040, or 2070, and (iii) invalid `VRAD`, `TEFF`, `LOGG`, or `FEH`. The GES DR3 comparison sample contains 5 010 stars.

LAMOST DR7. We used the data from the `dr7_v2.0_LRS_stellar.csv.gz` file, including the cross-match with the *Gaia* DR2 catalogue. The *Gaia* DR2 `source_id` were converted into *Gaia* EDR3 `source_id` using the table `gaiaedr3.dr2_neighbourhood`. For each LAMOST star that was observed multiple times (with all observations matching the same *Gaia* EDR3 star), the occurrence with the highest `snrg` was kept. Stars for which multiple LAMOST observations matched different *Gaia* EDR3 stars were removed. Duplicated *Gaia* EDR3 `source_id` and stars without a radial velocity measurement in *Gaia* DR3 were removed. Finally, only the

stars meeting the following quality criteria were considered: (i) `rv_error` ≥ 0, `snr` ≥ 0, `snrg` > 25, and `snri` > 25, and (ii) valid `rv`, `teff`, `logg`, and `feh`. The LAMOST DR7 comparison sample contains 1 791 438 stars.

RAVE DR6. The data (including the cross-match with the *Gaia* EDR3 catalogue) were downloaded from the tap server[4], from the tables `dr6_sparv`, `dr6_x_gaiaedr3`, `dr6_classification`, and `dr6_madera`. For the RAVE stars that were observed multiple times (with all observations matching the same *Gaia* EDR3 star and having the same value of the `flag_1` flag), the occurrence with the highest `snr_med_sparv` was kept. Stars for which multiple RAVE observations matched different *Gaia* EDR3 stars or that had different values of `flag_1` flag were removed. Duplicated *Gaia* EDR3 `source_id` and stars without a radial velocity measurement in *Gaia* DR3 were removed. Stars with `flag_1` set to e, b, p or c,w were removed. Finally, only the stars meeting the following quality criteria were considered: (i) absolute value of `correction_rv_sparv` < 10, `correlation_coeff_sparv` > 10, `hrv_error_sparv` < 8, `algo_con_madera` ∈ [0, 2, 3, 4], `snr_med_sparv` ≥ 20 and `fe_h_chisq_gauguin` < 1.4, and (ii) valid `hrv_sparv`, `teff_cal_madera`, `logg_cal_madera`, and `fe_h_gauguin`. The RAVE DR6 comparison sample contains 261 798 stars.

# Appendix D: Sample selection: Atmospheric parameter trends

The dependence on the atmospheric parameters of the systematic differences between *Gaia* DR3 and the comparison samples (see Appendix C) is studied in Sect. 6.2. To avoid mixing cross-dependences, specific samples were used for the effective temperature, the surface gravity, and the metallicity. They are described below.

The surface gravity and the effective temperature trends were assessed with samples of metal-rich giants and dwarfs, respectively. The selection was based on the atmospheric parameters provided by the different comparison catalogues. The metal-rich giants were selected according to $T_{\text{eff}} \leq 5500$ K, $\log g < 4.0$, and [Fe/H] ∈ [−0.5, 0.5] dex. The metal-rich dwarfs were selected according to [Fe/H] ∈ [−0.5, 0.5] dex and either $T_{\text{eff}} \leq 5500$ K and $\log g \geq 4.0$ or $T_{\text{eff}} > 5500$ K and $\log g \geq 3.5$. Some of the comparison catalogues contain only a few bright stars. To homogenise the bright limit in some way, the samples were trimmed at `grvs_mag` > 8.5 mag. The LAMOST sample was also restricted to `grvs_mag` < 12 mag to avoid the radial velocity offset that occurs at `grvs_mag` > 12.5 mag (see Sect. 6.1). Figure D.1 presents the Kiel diagrams of the comparison samples. The metal-rich giant and metal-rich dwarf samples are shown as salmon and blue dots, respectively.

In order to decouple the gravity-temperature trends, on the one hand, and the metallicity trends, on the other hand, the latter were assessed with groups of giants and dwarfs selected in narrow windows in the Kiel diagram. They are shown in Fig. D.2 as salmon (giants) and blue (dwarfs) dots, respectively. The magnitude cuts used for the gravity-temperature samples also apply here, that is, `grvs_mag` > 8.5 mag, and for the LAMOST catalogue, `grvs_mag` < 12 mag.

---

[3] https://archive.eso.org/wdb/wdb/adp/phase3_main/form?collection_name=GAIAESO&release_name=DR3

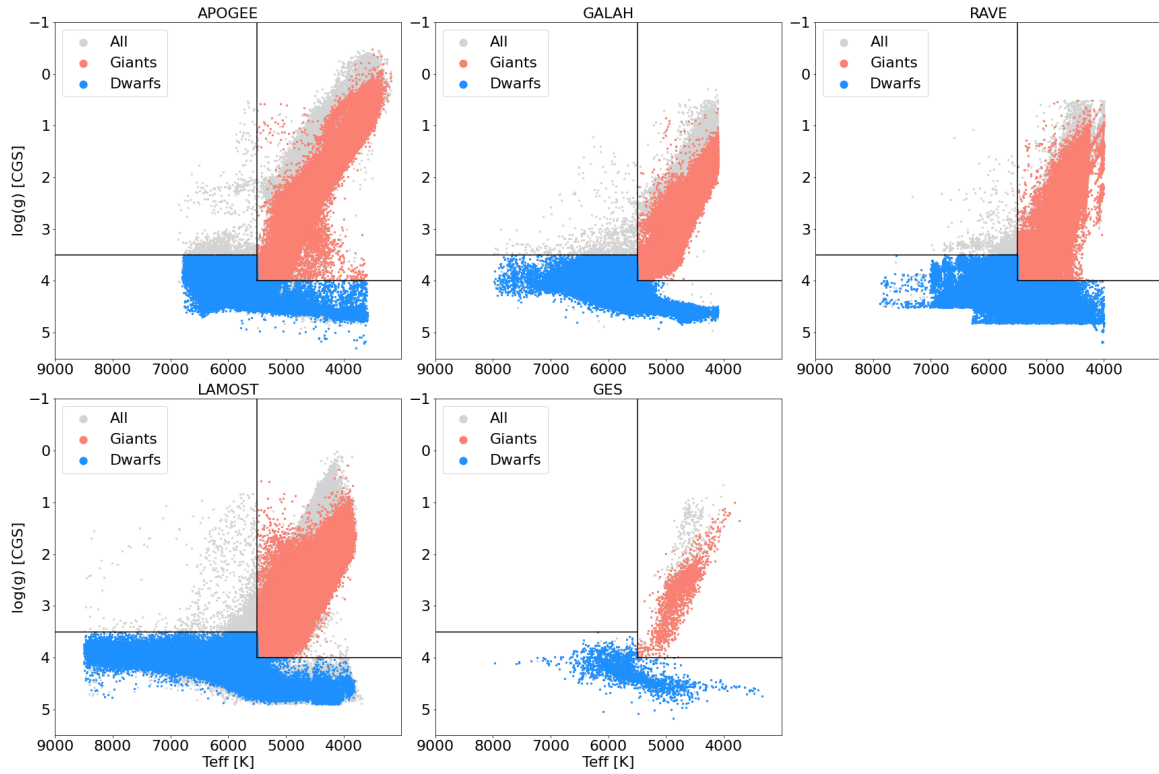[4] https://www.rave-survey.org/tap

**Fig. D.1.** Kiel diagrams of the comparison samples (see Appendix C). The metal-rich giant and metal-rich dwarf samples that were used to assess the radial velocity systematic differences as a function of surface gravity and effective temperature are shown as salmon and blue dots, respectively. The stars that were not selected in any of the samples are shown as grey dots.
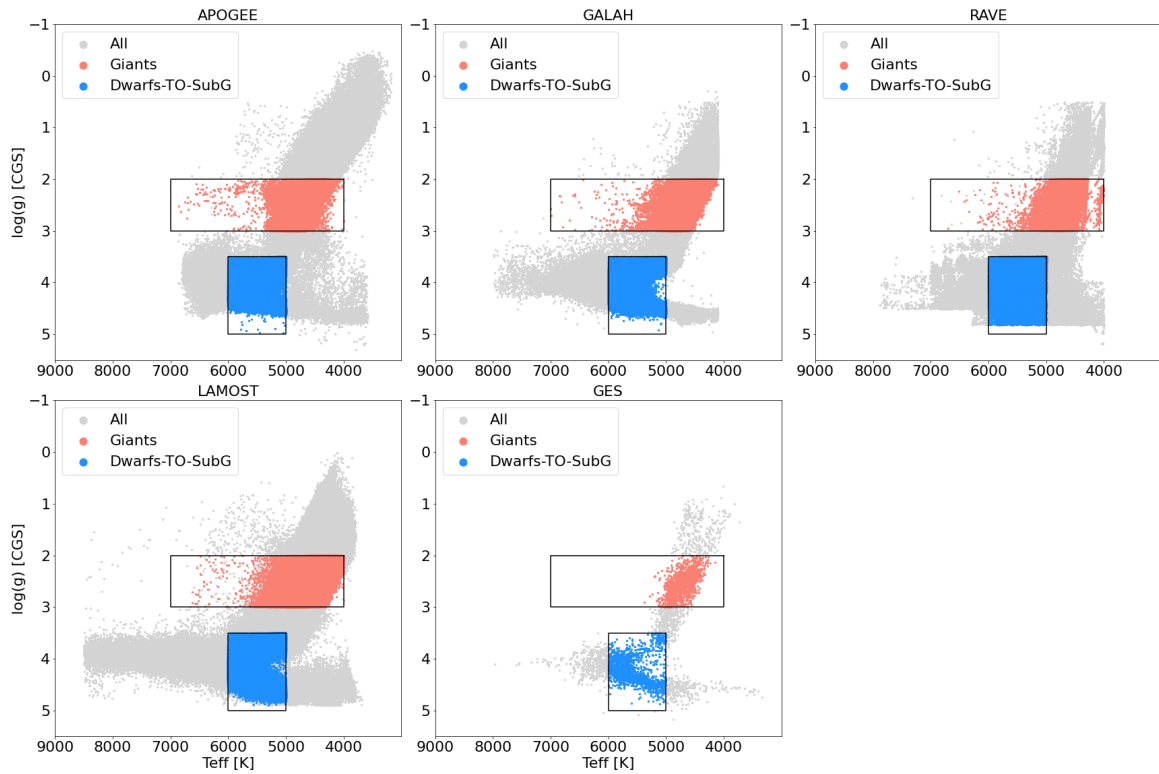


**Fig. D.2.** Kiel diagrams of the comparison samples (see Appendix C). The giant and dwarf samples that were used to assess the radial velocity systematic differences as a function of metallicity are shown as salmon and blue dots, respectively. The stars that were not selected in any of the samples are shown as grey dots.

## Appendix E: Sample selection: Formal uncertainties

In Sect. 7, the reliability of the formal uncertainties was assessed using the APOGEE DR17 comparison sample (see Appendix C). In order to minimise the number of radial velocity variable stars, two additional selection criteria were applied: at least four APOGEE measurements (NVISITS ≥ 4) and a scatter of the individual APOGEE radial velocities VSCATTER ≤ 0.5 km s$^{-1}$. The 94 309 stars meeting these criteria were further split into several dwarf and giant star samples: from g1 at the top of the giant branch, $\log g \in [-0.5, 1.0[$, to g4 at the bottom, $\log g \in [3.0, 4.0[$, and from d1 at the cool end of the main sequence, $T_{\rm eff} \in [3000, 4000[$ K, to d5 at the hot end, $T_{\rm eff} \in [7000, 8000[$ K. We note that the g4 and d3 samples partly overlap and therefore share some of their stars. The selections were based on the APOGEE DR17 effective temperatures and surface gravities. Fig. E.1 shows the selection of the giant and dwarf star samples in the Kiel diagram.
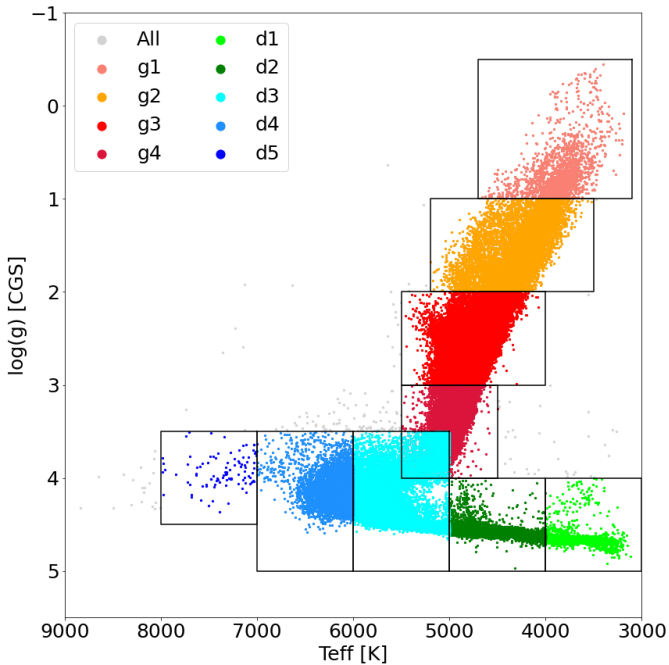


**Fig. E.1.** Selection in the Kiel diagram of the different giant and dwarf star samples that were used to assess the reliability of the formal uncertainties of the *Gaia* DR3 radial velocities. The stars that were not selected in any of the samples are shown as grey dots.

## Appendix F: Sample selection: Median formal precision

In Sect. 8, the median formal precision was estimated using the 33 812 183 stars with a radial velocity published in *Gaia* DR3. The parameters of the templates were used to split the data into several dwarf and giant star samples: from g1 at the top of the giant branch, rv_template_logg ∈ [−0.5, 0.5] to g4 at the bottom, rv_template_logg = 3.0 and from d1 at the cool end of the main sequence, rv_template_teff ≤ 3750 K, to d7 at the hot end, rv_template_teff ≥ 10000 K. Fig. F.1 shows the selection of the giant and dwarf star samples in the (rv_template_teff, rv_template_logg) plane.
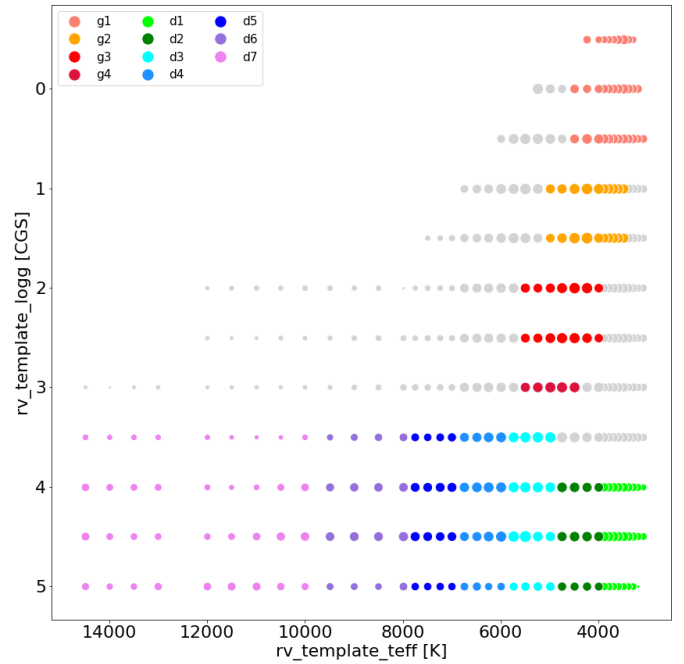


**Fig. F.1.** Selection in the (rv_template_teff, rv_template_logg) plane of the different giant and dwarf star samples we used to estimate the median formal precisions. The size of the dots is proportional to the number of stars with the combination of (rv_template_teff, rv_template_logg) parameters. The combinations of template parameters that were not selected in any of the samples are shown as grey dots.